GSA Books

Petrogenesis of the crystalline basement along the Western Gulf of Mexico: Post-collisional magmatism during the formation of Pangaea

--Manuscript Draft--

Manuscript Number:	GSABOOKS-D-17-00117R2
Full Title:	Petrogenesis of the crystalline basement along the Western Gulf of Mexico: Post-collisional magmatism during the formation of Pangaea
First Author:	Henry Eirian Coombs, Ph.D
Corresponding Author:	Henry Eirian Coombs, Ph.D Cardiff University Cardiff, Cardiff UNITED KINGDOM
Corresponding Author's Institution:	Cardiff University
Order of Authors:	Henry Eirian Coombs, Ph.D
	Andrew C Kerr, PhD
	James Pindell, PhD
	David Buchs, PhD
	Bodo Weber, PhD
	Luigi Solari, PhD
Keywords:	U-Pb dating; Major and trace element geochemistry; Lu-Hf isotopes; Pangaea; Post-collisional magmatism
Manuscript Classifications:	9.300: Geochemistry - Other; 41: Geochronology; 27.300: Petrology - Igneous; 37.600: Tectonics - Plate motions
Abstract:	The supercontinent of Pangaea formed through the diachronic collision of Laurussia and Gondwana during the Late Paleozoic. Whilst magmatism associated with its formation is well documented in the Variscan orogeny of Europe and Alleghanian orogeny of the USA, little is known about the Sonora orogeny of Northern Mexico. This paper reports geochronology (U-Pb zircon), whole rock geochemistry and Lu-Hf zircon isotope data on basement cores from the Western Gulf of Mexico, that are used to develop a tectonomagmatic model for pre- to post-Pangaea amalgamation. Our results suggest the existence of three distinct phases of magmatism, produced during different stages of continental assembly and disassembly. The first phase consists of Early Permian (294-274 Ma; n= 3) granitoids with geochemical signatures indicative of a continental arc tectonic setting. This phase formed on the margins of Gondwana during the closure of the Rheic Ocean, prior to the final amalgamation of Pangaea. It likely represents a lateral analogue of Late Carboniferous-Early Permian granitoids that intrude the Acatlán and Oaxacan Complexes. The second phase of magmatism includes Late Permian-Early Triassic (263-243 Ma; n= 13) granitoids with supra-subduction geochemical affinities. However, Lu-Hf isotope data indicate that these granitoids formed from crustal anatexis, with εHf values and two-step TDM(Hf) model ages comparable to the Oaxaquia continental crust that they intrude. This phase of magmatism is likely to be related to coeval granitoids in the Oaxaca area and Chiapas Massif. We interpret it to reflect late- to post-collisional magmatism along the margin of Gondwana following the assembly of Pangaea. Finally, the third phase of magmatism includes Early-Middle Jurassic (189-164 Ma; n= 2) mafic porphyries that could be related to the synchronous supra-subduction magmatism associated with the Nazas arc. Overall, our results are consistent with Pangaea assembly through diachronous collision of Laurussia and Gondwana during subduction of the Rheic Ocean. They suggest that post-orogenic magmatism in the western termination of the Rheic suture occurred under the influence of a Panthalassan subduction zone, before opening of the Gulf of Mexico.

Petrogenesis of the crystalline basement along the Western Gulf of Mexico: Post-collisional magmatism during the formation of Pangaea

Henry E. Coombs[1], Andrew C. Kerr[1], James Pindell[2], David Buchs[1], Bodo Weber[3] and Luigi Solari[4]

[1] *School of Earth and Ocean Sciences, Cardiff University Main Building, Park Place, Cardiff CF10 3AT, UK*

[2] *Tectonic Analysis Ltd, Chestnut House, Duncton, West Sussex GU28 0LH, UK*

[3] *Departamento de Geología, Centro de Investigación Científca y de Educación Superior de Ensenada (CICESE), Carretera Ensenada-Tijuana 3918, Zona Playitas, 22860 Ensenada B.C., Mexico*

[4] *Centro de Geociencias, Universidad Nacional Autónoma de México, Campus Juriquilla, 76001 Querétaro, Querétaro, Mexico*

ABSTRACT

The supercontinent of Pangaea formed through the diachronic collision of Laurussia and Gondwana during the Late Paleozoic. Whilst magmatism associated with its formation is well documented in the Variscan orogeny of Europe and Alleghanian orogeny of the USA, little is known about the Sonora orogeny of Northern Mexico. This paper reports geochronology (U-Pb zircon), whole rock geochemistry and Lu-Hf zircon isotope data on basement cores from the Western Gulf of Mexico, that are used to develop a tectonomagmatic model for pre- to post-Pangaea amalgamation. Our results suggest the existence of three distinct phases of magmatism, produced during different stages of continental assembly and disassembly. The first phase consists of Early Permian (294-274 Ma; n= 3) granitoids with geochemical signatures indicative of a continental arc tectonic setting. This phase formed on the margins of Gondwana during the closure of the Rheic Ocean, prior to the final amalgamation of Pangaea. It likely represents a lateral analogue of Late Carboniferous-Early Permian granitoids that intrude the Acatlán and Oaxacan Complexes. The second phase of magmatism includes Late Permian-Early Triassic (263-243 Ma; n= 13) granitoids with supra-subduction geochemical affinities. However, Lu-Hf isotope data indicate that these granitoids formed from crustal anatexis, with εHf values and two-step TDM(Hf) model ages comparable to the Oaxaquia continental crust that they intrude. This phase of magmatism is likely to be related to coeval granitoids in the Oaxaca area and Chiapas Massif. We interpret it to reflect late- to post-collisional magmatism along the margin of Gondwana following the assembly of Pangaea. Finally, the third phase of magmatism includes Early-Middle Jurassic (189-164 Ma; n= 2) mafic porphyries that could be related to the synchronous supra-subduction magmatism associated with the Nazas arc. Overall, our results are consistent with Pangaea assembly through diachronous collision of Laurussia and Gondwana during subduction of the Rheic Ocean. They suggest that post-orogenic magmatism in the western termination of the Rheic suture occurred under the influence of a Panthalassan subduction zone, before opening of the Gulf of Mexico.

INTRODUCTION

The Late Paleozoic is characterized by the formation of Pangaea through the collision and amalgamation of the Laurussia and Gondwana continents. This collision occurred diachronically, initiating in the east (Europe and Africa) during the Carboniferous (~340-330 Ma; Bussien et al., 2011), and terminating in the west (Mexico) during the Early Permian (~280 Ma; Pindell and Dewey, 1982; Pindell, 1985; Ross, 1986; Viele and Thomas, 1989; Sedlock et al., 1993; Dickinson and Lawton, 2001). The suture of this major collision zone is recorded in the Sonora-Marathon-Ouachita-Alleghanian orogenies of Northern Mexico and the USA, and the Variscan orogeny of Europe.

Existing geochronological and geochemical data document a complex tectonic history of the formation of Pangaea. The collision of Laurussia and Gondwana during the Variscan orogeny of Europe is associated with three distinct, syn- (340-330 Ma), late- (310 Ma) and post-collisional magmatic phases (Schaltegger, 1997; Bussy et al., 2000; von Raumer and Bussy, 2004; Bussien et al., 2011). Further west, the Laurussia-Gondwana collision along the Ouachita-Marathon-Alleghanian orogenies did not occur until the Late Carboniferous-Early Permian, with arc rocks relating to the closure of the Rheic Ocean dating to 325 Ma (U-Pb zircon; Shaulis et al., 2012) and syn-, late- and post-collisional granitoids dating to 300-275 Ma (Walsh et al., 2007; Heatherington and Mueller, 2010; Mueller et al., 2014). In Northeast Mexico, the Sonora segment of the Laurussia-Gondwana collision could provide important constraints on the timing and mode of assembly and disassembly of Pangaea. This segment includes a continuous 3000 km Palaeozoic carbonate continental shelf with consistent stratigraphic and structural characteristics that extend from Sonora to the Southern USA (Poole et al., 2005). However, very little is known about orogenic magmatism in this area. Yet, understanding the mechanics of the collision in the Sonora segment is important because it likely marks the latest phase of the Laurussia-Gondwana collision and final amalgamation of Pangaea.

Herein, we present new whole rock geochemical data, U-Pb zircon geochronology and Lu-Hf zircon isotope data for well cuttings from the crystalline basement of the Western Gulf of Mexico. Jurassic plate reconstructions (Pindell and Kennan, 2009) of Western Pangaea place the area of the Western Gulf of Mexico close to the Ouachita-Sonora suture zone. Based on these new data, we propose a pre- to post-collisional model for magmatism associated with the formation of Pangaea along the Sonora segment of the Pangaea suture zone.

GEOLOGICAL SETTING

Crystalline Basement of the Western Gulf of Mexico

Ages for the crystalline basement (cores) of the Western Gulf of Mexico have previously been presented in an internal Petróleos Mexicanos (PEMEX) report by Lopez-Ramos et al. (1979). The method of dating was primarily K-Ar on biotite or potassium feldspars, and yielded a wide range of heterogeneous ages from the Neoproterozoic to Early Cretaceous (Table. 1). A detailed description of the crystalline basement of Mexico can be found in Ortega-Gutiérrez et al. (2014), however we present below a brief outline of the major basement-forming Proterozoic-Jurassic igneous events in Mexico.

Oaxaquia

Oaxaquia or the Oaxaquia microcontinent is associated with a Grenvillian phase of magmatism and is thought to underlie the majority of Gondwana derived Mexico. Oaxaquia was first described in Ortega-Gutiérrez et al. (1995), with outcrops found in the Oaxacan Complex, Novillo Gneiss, Huiznopala Gneiss and Guichicovi Complex (Fig. 1A).

The oldest reported ages for Oaxaquia range between 1.5 and 1.4 Ga (U-Pb zircons in orthogneiss and migmatites; Solari et al., 2003; Schulze, 2011; Weber and Schulze, 2014). These ages have been associated with an early island arc known as Proto-Oaxaquia (Weber and Schulze, 2014). A later and more prevalent pulse of island arc magmatism, possibly associated with back-arc magmatism, occurred between 1.3 and 1.2 Ga (Lawlor et al., 1999; Keppie et al., 2001; Keppie, 2004; Weber et al., 2010; Weber and Schulze, 2014).

Migmatization (Olmecan event) occurred in Oaxaquia ca. 1.1 Ga (Solari et al., 2003), which has been linked to either back-arc extension (Keppie et al., 2001, 2003; Keppie, 2004) or a compressional event during accretion of the microcontinent to Amazonia. Following migmatization, an anorthosite-mangerite-charnockite-granite (AMCG) suite was emplaced ca.

1012 Ma (Solari et al., 2003), which has also been linked to back-arc extension (Solari et al., 2003; Keppie et al., 2004) or Oaxaquia-Amazonia collision (Weber et al., 2010).

Acatlán Complex

The Acatlán Complex of Southern Mexico (Fig. 1A) is one of the few areas exposed in the region that preserves Paleozoic rocks. It is composed of a complex succession of deformed high-pressure (HP) metamorphic rocks, including eclogites and blueschists, deformed granitoids and metasedimentary rocks. The origin of these Paleozoic rocks is still debated, with some studies proposing formation at an active continental margin along Laurentia (Talavera-Mendoza et al., 2005; Vega-Granillo et al., 2007 and 2009) or Gondwana (van der Lelij et al., 2016). Other models suggest that the Acatlán Complex formed along a passive margin of Gondwana, with HP metamorphic rocks extruded into the upper plate during the Carboniferous (Keppie et al., 2008 and 2012; Ortega-Obregón et al., 2009 and 2014; Estrada-Carmona et al., 2016).

Regardless of how the Acatlán Complex was formed, it is generally agreed that it was emplaced along a continental margin (either Laurussia or Gondwana). This indicates that it could have been proximal to the Sonora segment of the collision zone during the final amalgamation of Pangaea.

Carboniferous-Triassic Magmatism

Late Carboniferous-Early Triassic granitoids can be found across Mexico, including the Sierra Pinta, Chiapas Massif and intrusions into the Acatlán and Oaxacan Complexes (Fig. 1A; Table. 1). One interpretation of these igneous rocks is that they formed in a continental arc system, associated with the eastward dipping subduction of the Panthalassa Ocean beneath Pangaea (Keppie et al., 2004; Arvizu and Iriondo, 2011; Kirsch et al., 2012; Ortega-Obregón et al., 2014). Alternatively, the igneous event could be linked to the final amalgamation of Pangaea (Yañez et al., 1991; Elías-Herrera et al., 2005).

Paleogeographic reconstructions of Pangaea (Pindell and Kennan, 2009) indicate a close proximity between Mexico and South America at this time. This suggests that the Carboniferous-Triassic magmatism in Mexico may be associated with Permian-Triassic arc rocks that are found in Ecuador, Venezuela and Colombia (Vinasco et al., 2006; Cochrane et al., 2014; Spikings et al., 2015).

Nazas Arc

Early Jurassic magmatism in Mexico is most commonly associated with the Nazas arc system (Fig. 1A; Dickinson and Lawton, 2001; Lawton and Molina Garza, 2014). Volcanic exposures outcrop in northern Central Mexico (Barboza-Gudiño et al., 2008) and possibly extend as far south as the Chiapas Massif (Godínez-Urbán et al., 2011; Dickinson and Molina Garza, 2014). Plutonic equivalents of these Jurassic arc rocks can be found in the Northeastern Mexico (Ortega-Gutíerrez et al., 2014).

SAMPLES AND PETROGRAPHY

Samples for this study were supplied by PEMEX and extracted from wells on basement highs along the Western Gulf of Mexico (Tamaulipas Arch, Tuxpan and Santa Ana). The wells occur at regular intervals, over an area of ~120,000 km^2, and therefore provide a good representation of the basement throughout Eastern Mexico (Fig. 1B).

Petrographic observations (Fig. 2 A-D) reveal that the majority of the samples are phaneritic with granodiorite-granite compositions. The main mineral assemblages include quartz-feldspars-biotite±hornblende±muscovite. Common accessory minerals include zircon, apatite, titanite and opaques. Minor (common) to extensive (rare) hydrothermal alteration in the granitoids is evidenced by sericitized feldspars, chloritized biotite, calcite and epidote. There is little evidence from the petrography of significant deformation affecting the granitoids.

A subset of samples (Muro-2 and Tlapacayon-1) display finer phaneritic/porphyritic textures, typical of hypabyssal rocks (Fig. 2 E-F). This suggests that they emplaced at a shallower depth than the coarser plutonic samples described above, or represent small intrusive bodies. These hypabyssal rocks are characterized by more mafic mineral assemblages, with minor clinopyroxene and olivine (partially altered to iddingsite) and no quartz.

GEOCHRONOLOGY

Analytical Methods

Geochronological data (U-Pb zircon) were obtained by laser ablation inductively coupled plasma mass spectrometry (LA-ICP-MS) at the Laboratorio de Estudios Isotópicos (LEI), Centro de Geociencias, Universidad Nacional Autonóma de México, Querétaro, Mexico. A Thermo X-ii quadrupole ICP-MS was used coupled with a resolution M050 excimer laser ablation workstation. A cathodoluminescence (CL) study before analysis identified suitable target areas in the zircons, avoiding core-rim transitions, cracks and inclusions. During analysis, a 30 μm laser spot was employed, with the Plešovice zircon (Sláma et al. 2008) being used as a bracketing standard. NIST 610 glass was used to recalculate elemental concentrations and ^{29}Si was used as an internal standard. Following analysis, the data were reduced using an algorithm slightly modified from Solari and Tanner (2011) and then exported into Excel® where concordia plots and weighted mean age calculations were constructed using Isoplot (Ludwig, 2012) version 4.15. Where necessary, a correction for common lead was applied using the algebraic method of Andersen (2002). Further details on the equipment used and analytical procedures can be found in Solari et al. (2010).

Results

Zircons were successfully extracted and analyzed in 18 samples from wells along the Western Gulf of Mexico. Th/U ratios (Fig. 3A-R) indicate that the zircons are dominantly magmatic in origin, with the majority of the analyzed grains falling between 0.1-1. The CL study (Fig. 4A-R) supports this interpretation, with most of the zircons displaying typical igneous textures (oscillatory and sector zoning). Furthermore, the CL images reveal core and rim relationships and resorption features in many of the samples (indicated below when present).

Depending on the age of the zircons, results of the analysis have been graphically presented in either a Tera-Wasserburg plot in association with a ^{206}Pb/^{238}U weighted-mean age calculation or Wetherill Concordia diagram in association with a ^{207}Pb/^{206}Pb weighted-mean age calculation. The ^{206}Pb/^{238}U weighted-mean age calculation is more precise with Phanerozoic zircons, whereas the ^{207}Pb/^{206}Pb weighted-mean age calculation is more suitable for Precambrian zircons (Jackson et al., 2004; Ludwig, 2012).

Our data reveal three apparent phases of magmatism: 1) Early Permian (294-274 Ma; n= 3), 2) Late Permian-Early Triassic (263-243 Ma; n= 13) and 3) Early-Middle Jurassic (188-164 Ma; n= 2) (Table. 2). Significantly, these results indicate that the basement of the Western Gulf of Mexico is characterized by magmatic phases more consistent than previously suggested by K-Ar dating (Lopez-Ramos, 1979; Table. 1). The previous ages of Lopez-Ramos (1979) have been included in the text below for comparison, where available.

Early Permian

***Pinonal-1 (1)*:** The first sample from the Pinonal-1 well is a biotite granitoid that has undergone subsequent alteration. It contains subhedral zircons that are 200-800 μm along their longest axis, with aspect ratios of 2:1-5:1, and CL textures that display no evidence of inherited cores (Fig. 4A).

Of the 43 analyzed zircons, 36 were selected for age calculations (< 20% discordant, < 5% error and < 5% inversely discordant; Fig. 3A). A weighted-mean calculation for the zircons yields an age of 294.1 ± 3.4 Ma (n= 35; MSWD= 1.15; one age rejected by the algorithm), which can be interpreted as the igneous crystallization age of the sample.

Arenque-22: The sample from the Arenque-22 well is a biotite granite, containing subhedral zircons that are 100-300 µm along their longest axis, with aspect ratios of 2:1-5:1, and CL textures that reveal core and rim relationships (Fig. 4B).

Of the 40 analyzed zircons, 36 were selected for age calculations (< 20% discordant, < 5% error, < 5% inversely discordant; Fig. 3B). One inherited core was analyzed and yielded a Late Carboniferous age of 322 ± 11 Ma. A weighted-mean calculation for the main population of zircons yields an age of 293.5 ± 3.7 Ma (n= 34; MSWD= 1.4; two ages rejected by the algorithm), which can be interpreted as the igneous crystallization age of the sample.

Paso de Oro-101: The sample from the Paso de Oro-101 well is a granodiorite containing prismatic, euhedral zircons that are 100-600 µm along their longest axis, with aspect ratios of 2:1-8:1, and CL textures that display no evidence of inherited cores (Fig. 4C). The basement from this well has previously been dated to 258 ± 11 Ma (K-Ar biotite; Lopez-Ramos, 1979).

Of the 26 analyzed zircons, 19 were selected for age calculations (< 20% discordant, < 5% error, < 5% inversely discordant; Fig. 3C). A weighted-mean calculation yields an age of 274.2 ± 3.5 Ma (n= 18; MSWD= 0.77; one age rejected by the algorithm), which can be interpreted as the igneous crystallization age of the sample.

Late Permian-Early Triassic

Benemerito-1: The sample from the Benemerito-1 well is a granite containing prismatic, euhedral zircons that are 80-400 µm along their longest axis, with aspect ratios of 2:1-6:1. The CL textures reveal core and rim relationships and evidence for partial resorption of the zircons (Fig. 4D). The basement from this well has previously been dated to 916 ± 35 Ma and 203 ± 10 Ma (method unknown; Lopez-Ramos, 1979).

Relationships between U concentrations and $^{238}U/^{206}Pb$ ratios indicate that partial metamictization of the zircons has occurred (Fig. 3D). Therefore, zircons with high U concentrations have been disregarded.

Of the 35 analyzed zircons, 11 were selected for age calculations (< 20% discordant, < 5% error, < 5% inversely discordant and < 1000 ppm U; Fig. 3D). One inherited core was analyzed and yielded a Mesoproterozoic age of 1266 ± 93 Ma. A weighted-mean calculation for the youngest population of zircons yields an age of 245.4 ± 4.6 Ma (n= 10; MSWD= 1.8), which can be interpreted as the igneous crystallization age of the sample.

Trincheras-1: The sample from the Trincheras-1 well is a biotite granite, containing euhedral to subhedral zircons that are 100-300 µm along their longest axis, with aspect ratios of 2:1-5:1, and CL textures that reveal core and rim relationships (Fig. 4E). The basement from this well has previously been dated to 147 ± 5 Ma (K-Ar biotite; Lopez-Ramos, 1979).

Relationships between U concentrations and $^{238}U/^{206}Pb$ ratios indicate that partial metamictization of the zircons has occurred (Fig. 3E). Therefore, zircons with high U concentrations have been disregarded.

Of the 40 analyzed zircons, 33 were selected for age calculations (< 20% discordant, < 5% error, < 5% inversely discordant and < 1000 ppm U; Fig. 3E). Four inherited cores were analyzed and yielded Proterozoic (1018 ± 82 Ma & 755 ± 8 Ma) and Early Permian (288 ± 5 Ma

& 289 ± 4 Ma) ages. A weighted-mean calculation for the youngest population of zircons yields an age of 254.6 ± 3.4 Ma (n= 29; MSWD= 3.4; three ages rejected by the algorithm), which can be interpreted as the igneous crystallization age of the sample.

Linares-1: The sample from the Linares-1 well is a granodiorite, containing euhedral to subhedral zircons that are 150-250 µm along their longest axis, with aspect ratios of 2:1-7:1, and CL textures that reveal core and rim relationships (Fig. 4F). The basement from this well has previously been dated to 112 ± 5 Ma (K-Ar biotite; Lopez-Ramos, 1979).

Of the 40 analyzed zircons, 31 were selected for age calculations (< 20% discordant, < 5% error, < 5% inversely discordant; Fig. 3F). One inherited core was analyzed and yielded a Late Carboniferous (304 ± 8 Ma) age (Supplementary Material 1). A weighted-mean calculation for the concordant grains yields an age of 254.3 ± 4.6 Ma (n= 29; MSWD= 4.0; one age was rejected by the algorithm), which can be interpreted as the igneous crystallization age of the sample.

Chaneque-1: The sample from the Chaneque-1 well is a granitoid that has undergone subsequent hydrothermal alteration. It contains subhedral zircons that are 150-300 µm along their longest axis, with aspect ratios of 3:1-7:1, and CL textures that display no evidence of inherited cores (Fig. 4G). The basement from this well has been previously dated to 133 ± 5 Ma (K-Ar K-feldspar; Lopez-Ramos, 1979).

Of the 38 analyzed zircons, 28 were selected for age calculations (< 20% discordant, < 5% error, < 5% inversely discordant; Fig. 3G). A weighted-mean calculation for the zircons yields an age of 243.4 ± 2.8 Ma (n= 26; MSWD= 1.9; two ages were rejected by the algorithm), which can be interpreted as the igneous crystallization age of the sample.

Nayade-1: The sample from the Nayade-1 well is a biotite granite that has undergone subsequent hydrothermal alteration. It contains subhedral zircons that are 100-400 µm along their longest axis, with aspect ratios of 1:1 to 5:1, and CL textures that reveal core and rim relationships (Fig. 4H).

It is apparent from relationships between U concentrations and $^{238}U/^{206}Pb$ ratios that partial metamictization of the zircons has occurred (Fig. 3H). Therefore, zircons with high U concentrations have been disregarded.

Of the 35 analyzed zircons, 16 were selected for age calculations (< 20% discordant, < 5% error, < 5% inversely discordant and < 1000ppm U; Fig. 3H). Three inherited cores were analyzed and yielded Neoproterozoic (558 ± 4 Ma), Cambrian (538 ± 6 Ma) and Devonian (397 ± 6 Ma) ages (Supplementary Material 1). A weighted-mean calculation for the youngest population of zircons yields an age of 257 ± 5.2 Ma (n= 13; MSWD= 3.7), which can be interpreted as the igneous crystallization age of the sample.

Tamaulipas-103: The sample from the Tamaulipas-103 is a granodiorite containing subhedral zircons that are 150-400 μm along their longest axis, with aspect ratios of 2:1-6:1, and CL textures that reveal core and rim relationships (Fig. 4I).

Of the 37 analyzed zircons, 28 were selected for age calculations (< 20% discordant, < 5% error, < 5% inversely discordant; Fig. 3I). Two inherited cores were analyzed and yield an Early Permian age (282 ± 10 Ma and 279 ± 8 Ma; Supplementary Material 1). A weighted-mean calculation for the youngest population of zircons yields an age of 247.9 ± 4.0 Ma (n= 26; MSWD= 1.8), which can be interpreted as the igneous crystallization age of the sample.

Erizo-1: The sample from the Erizo-1 well is a granite that has undergone subsequent hydrothermal alteration. It contains subhedral zircons that are 100-300 μm along their longest axis, with an aspect ratio of 2:1-5:1, and CL textures that display no evidence of inherited cores (Fig. 4J).

It is apparent from relationships between U concentrations and the $^{238}U/^{206}Pb$ ratio that partial metamictization of the zircons has occurred (Fig. 3J). Therefore, those with high U concentrations have not been considered in age calculations.

Of the 49 analyzed zircons, 38 were selected for age calculations (< 20% discordant, < 5% error, < 5% inversely discordant, < 800 ppm U; Fig. 3J). A weighted-mean calculation for the concordant grains yields an age of 249.8 ± 2.7 Ma (n= 37; MSWD= 1.8; one age was rejected by the algorithm), which can be interpreted as the igneous crystallization age of the sample.

Pinonal-1 (2): The second sample from the Pinonal-1 well is a granodiorite that has undergone subsequent hydrothermal alteration. It contains euhedral to subhedral zircons that are 200-400 μm along their longest axis, with aspect ratios of 2:1-10:1, and CL textures that reveal core and rim relationships (Fig. 4K).

Of the 31 analyzed zircons, 27 were selected for age calculations (< 20% discordant, < 5% error, < 5% inversely discordant; Fig. 3K). Three inherited cores were analyzed and yield Mesoproterozoic (1235 ± 153 Ma), Cambrian (509 ± 7.8 Ma) and Ordovician (478 ± 6.8 Ma) ages (Supplementary Material 1). A weighted-mean calculation for the youngest population of zircons yields an age of 249.8 ± 3.2 Ma (n= 22; MSWD= 1.6; two ages were rejected by the algorithm), which can be interpreted as the igneous crystallization age of the sample.

Cupelado-1: The sample from the Cupelado-1 well is a biotite granitoid, containing euhedral to subhedral zircons that are 100-300 μm along their longest axis, with aspect ratios of 1:1-5:1. The CL images reveal distinct populations of igneous zircons that are defined by their luminescence, with evidence of resorption in some of the grains (Fig. 4L).

Of the 19 analyzed zircons, 17 were selected for age calculations (< 20% discordant, < 5% error, < 5% inversely discordant; Fig. 3L). These 14 ages can be sub-divided into three groups on the basis of their age. The weighted-mean calculation for the oldest population of zircons yield a Mesoproterozoic age of 1418 ± 41 Ma (n= 7; MSWD= 0.28; one age was rejected by the algorithm). A second population of zircons yield an Early Permian age of 284.7 ± 7.7 Ma (n= 4; MSWD= 0.11). The youngest population of zircons yields a Late Permian age of 262.7 ± 4.5 Ma (n= 5; MSWD= 0.86), which can be interpreted as the igneous crystallization age of the sample.

Plan de Las Hayas-1 (1): The first sample from the Plan de Las Hayas-1 well is a granodiorite, containing subhedral, prismatic zircons that are 80-200 μm along their longest axis, with aspect ratios of 1:1-4:1, and CL textures that display no evidence of inherited cores (Fig. 4M). The basement associated with this well has been previously dated to 312 ± 25 Ma (K-Ar K-feldspar; Lopez-Ramos, 1979).

Of the 29 analyzed zircons, 24 were selected for age calculations (< 20% discordant, < 5% error, < 5% inversely discordant; Fig. 3M). A weighted-mean calculation for the concordant grains yields an age of 261.0 ± 4.1 Ma (n= 24; MSWD= 2.8), which can be interpreted as the igneous crystallization age of the sample.

Plan de las Hayas-1 (2): The second sample from the Plan de Las Hayas-1 well is a quartz diorite, containing euhedral, prismatic zircons that are 150-250 μm along their longest axis, with aspect ratios of 2:1-10:1. The CL images reveal complex textures, with evidence of the zircons being partially resorbed but no inherited cores (Fig. 4N). The basement associated with this well has previously been dated to 312 ± 25 Ma (K-Ar K-feldspar; Lopez-Ramos, 1979)

Of the 30 zircons analyzed, 25 were selected for age calculations (< 20% discordant, < 5% error, < 5% inversely discordant; Fig. 3N). A weighted-mean calculation for the zircons yields an age of 251.7 ± 5.2 Ma (n= 24; MSWD= 3.0; one age was rejected by the algorithm), which can be interpreted as the igneous crystallization age of the sample.

Paso de Ovejas-2: The sample taken from the Paso de Ovejas-2 well is a quartz monzodiorite. It contains elongated, euhedral, prismatic zircons that are 100-300 µm along their longest axis, with aspect ratios of 2:1-10:1. The CL images reveal core and rim relationships and resorption features (Fig. 4O).

Of the 30 analyzed zircons, 23 were selected for age calculations (< 20% discordant, < 5% error, < 5% inversely discordant; Fig. 3O). Two inherited cores were analyzed and yield an Early Permian age (297 ± 9 Ma and 298 ± 7 Ma; Supplementary Material 1). A weighted-mean calculation for the youngest population of zircons yields an age of 256.7 ± 5.5 Ma (n= 21; MSWD= 2.3; two ages were rejected by the algorithm), which can be interpreted as the igneous crystallization age of the sample.

Orizaba-1: The sample from the Orizaba well is a monzo-granite that contains euhedral to subhedral zircons that are 100-400 µm along their longest axis, with aspect ratios of 2:1-5:1. The CL images reveal zircons that are characterized by igneous rims and cores that are both igneous and metamorphic in origin (Fig. 4P).

Of the 52 analyzed zircons, 35 were selected for age calculations (< 20% discordant, < 5% error, < 5% inversely discordant; Fig. 3P). Weighted-mean calculation for the oldest population of inherited cores reveal a Mesoproterozoic age of 1149 ± 34 Ma (n= 9; MSWD= 1.02), characterized CL textures typical of igneous zircons (Fig. 4P; oscillatory zoning). A second population of inherited cores yield a Neoproterozoic age of 970 ± 53 Ma (n= 9; MSWD= 1.2) and CL textures more typical of metamorphic zircons (Fig. 4P; homogeneous, with no zoning). A weighted mean calculation for the youngest population of zircons yields an age of 261 ± 4.9 Ma (n= 17; MSWD= 4.4), which can be interpreted as the igneous crystallization age of the sample.

Jurassic

Muro-2: The sample from the Muro-2 well is a micro diorite and contains euhedral-subhedral zircons that are 50-120 µm along their longest axis, with aspect ratios of 2:1-7:1. The CL images reveal core and rim relationships and evidence of resorption features (Fig. 4Q). Basement samples from this well have previously been dated to 153 ± 11 Ma and 178 ± 11 Ma (K-Ar biotite; Lopez-Ramos, 1979).

Of the 21 analyzed zircons, 13 were selected for age calculations (< 20% discordant, < 5% error, < 5% inversely discordant; Fig. 3Q). Two inherited cores were analyzed and yielded Mesoproterozoic (1430 ± 24 Ma) and Devonian (398 ± 3.2 Ma) ages (Supplementary Material 1). A weighted-mean calculation for the youngest population of zircons yields an age of 188.3 ± 4.0 Ma (n= 11; MSWD= 5.4), which can be interpreted as the igneous crystallization age of the sample. The high MSWD recorded in this sample is likely to be caused by common lead contamination along fractures, evidenced by the bright areas of the zircons (along their c-axis) in the CL images (Fig. 4Q).

Tlapacoyan-1: The sample from the Tlapacoyan-1 well is a trachyte that contains euhedral to subhedral zircons that are 80-200 µm along their longest axis, with aspect ratios of 2:1-7:1, and CL textures that reveal core and rim relationships (Fig. 4R). The basement from this well has previously been dated to 179 ± 14 Ma (K-Ar on biotite; Lopez-Ramos, 1979).

Of the 30 analyzed zircons, 19 were selected for age calculations (< 20% discordant, < 5% error, < 5% inversely discordant; Fig. 3R). Two inherited cores were analyzed and yielded Neoproterozoic (838 ± 60 Ma) and Late Permian (263 ± 7 Ma) ages (Supplementary Material 1). A weighted mean calculation for the youngest population of zircons yields an age of 163.5 ± 4.7

Ma (n= 16; MSWD= 3.6; one age was rejected by the algorithm), which can be interpreted as the igneous crystallization age of the sample.

MAJOR AND TRACE ELEMENT GEOCHEMISTRY

Analytical Methods

Sample preparation and analysis were carried out at Cardiff University, Wales. Veins and weathered surfaces were first removed and then the samples were crushed using a steel jaw crusher and powdered using an agate Tema® mill. Powdered samples were then digested by fusion in platinum crucibles on a Claisse Fluxy automated fusion system using 0.1 ± 0.0005g of sample with 0.4 ± 0.0005g of lithium tetraborate flux. Major element abundances were determined using a JY Horiba Ultima 2 inductively coupled plasma optical emission spectrometer (ICP-OES), whilst trace element abundances were measured using a Thermo X7 series ICP-MS. Accuracy and precision of the data were assessed using the international reference material NIM-G. Further details on analytical procedures can be found in McDonald and Viljoen (2006).

Results

The geochronological results reveal the more mafic, hypabyssal basement samples from the Muro-2 and Tlapacayon-1 wells to be Jurassic in age. It is therefore apparent that they are unrelated to the intermediate-felsic intrusive rocks of the Western Gulf of Mexico, which yield Permian-Triassic ages. The geochemical analysis of this study has focused on the more prevalent Permian basement, but it is possible that the few Jurassic samples are related to coeval volcanism associated with the Nazas arc discussed above.

Element Mobility

Petrographic observations indicate that the majority of the samples are relatively unaltered. These observations are supported by low loss of ignition (LOI) values that range between 0.60 and 4.17 wt.% (Table. 3). The samples that displayed signs of hydrothermal alteration in thin section can be associated with the highest LOI values (5.42-6.84 wt.%).

Assessing mobility using conventional element mobility plots (i.e. an immobile element such as Zr plotted against other elements) is not suitable in our study. These plots work under the assumption of a homogenous source region, but our samples have a large spatial distribution and temporal span that make the validity of this assumption unlikely. However, petrographic observations coupled with low LOI values suggest that there has not been substantial element mobility in most of the studied samples.

Major Elements and Classification

Major element compositions for the majority of the Early Permian, Late Permian-Early Triassic and undated samples are similar and are typical of intermediate-evolved granitoids; with SiO_2, TiO_2 and MgO values ranging between 61.1-74.4 wt.%, 0.1-0.8 wt.% and 0.1-4.2 wt.% respectively (Table. 3). This is supported by the Quartz-Alkali Feldspar-Plagioclase-Feldspathoid (QAPF) and Total-Alkali Silica (TAS) classification diagrams (Fig. 5), which show that the samples are predominantly granodiorite-granite in composition. Two of the Late Permian granitoids that yield the highest LOI values (Chaneque N6F1C2 and Pinonal N2F11C2) have anomalous major element values e.g. SiO_2, (Fig. 5). This indicates that the major elements in these samples have been mobilized during subsequent alteration.

Trace Elements

Chondrite normalized rare earth element (REE) and normal mid-ocean ridge basalt (N-MORB) normalized multi-element diagrams are shown in Fig. 6. The Early Permian, Late

Permian-Early Triassic and undated crystalline basement of the Western Gulf of Mexico displays enriched REE trends (x27, x31 and x40 chondrite, respectively), which have enriched chondrite normalized LREE signatures when compared to the HREE (La/Sm_{Ch}= 2.6-7.8). The MREEs are commonly defined by concave trends (Dy/Dy*= 0.42-0.80) and the HREEs are flat to positively sloping (Ho/Lu_{Ch} 0.54-3.19). Enrichment in Th, as well as negative anomalies in Nb (Nb/Nb*= 0.03-0.26), Ta (Ta/Ta*= 0.05-0.39) and Ti (Ti/Ti*= 0.14-0.53) are prevalent throughout the samples.

The basement samples from the Western Gulf of Mexico have been compared in tectonic discrimination diagrams (Fig. 7) with Carboniferous-Triassic granitoids from the Totoltepec Pluton, Cozahuico granite, and La Carbonera stock of Southern Mexico (Fig. 1; Kirsch 2012), the Chiapas Massif of Southeastern Mexico (Fig. 1; Weber et al., 2005; Estrada-Carmona et al., 2012) and the Colombian Andes (Vinasco et al., 2006; Cochrane et al., 2014). Significant overlap is observed between the Late Permian-Early Triassic crystalline basement of the Western Gulf of Mexico and granitoids of comparable ages in the Chiapas Massif, indicating similar sources and possible tectonomagmatic setting. The Early Permian crystalline basement displays similar trends, although there are some examples that appear to have more of an affinity to the Carboniferous-Permian granitoids of the Totoltepec Pluton (Fig. 7). These older granitoids plot firmly in the volcanic arc fields in all of the discrimination plots, whereas the younger Permo-Triassic granitoids plot closer to the syn-collisional boundary. The Permo-Triassic granitoids from the Colombian Andes do not show such strong relationships with the Western Gulf of Mexico and Chiapas, but some overlap is still observed.

The tectonic discrimination diagrams suggest an affiliation to volcanic arc magmatism with potentially a minor syn-collisional component in some of the younger Permo-Triassic granitoids.

However, these diagrams are not effective in defining all tectonic settings, e.g. granitoids that form in post-collisional environments (Pearce et al., 1984), due to the heterogeneous nature of the magmas that form in these settings. This will be discussed in more detail below.

ZIRCON ISOTOPE GEOCHEMISTRY

Analytical Methods

Chemical preparation and element separation were carried out on PicoTrace® clean benches at Laboratorio Ultralimpio de Geología Isotópica, Departamento de Geología (CICESE). Individual zircon grains, previously dated by LA-ICP-MS (Fig. 4), were removed from mounts under a stereomicroscope with a needle and weighed into microcapsules. The zircons were then washed several times with warm 7 M HNO_3, and then with cold, concentrated HNO_3. Next, a ^{180}Hf-^{176}Lu spike was pipetted into the microcapsules before adding about 0.5 ml of concentrated HF. Microcapsules were heated with HF as a pressure medium in a Parr® bomb for 6 days at 180°C. After digestion, the samples were dried down on a hotplate. Heating the closed microcapsules overnight in 6 M HCl and then repeating the drying process facilitated sample-spike equilibration. Sample residues were then dissolved in ~0.5 ml of 1 M HCl and loaded to microcolumns filled with ~160 μl of Eichrom Ln-spec® resin. Lu+Yb, and Hf were eluted following a single column separation procedure adopted from Nebel-Jacobsen et al. (2005).

The determination of Lu and Hf isotope ratios was carried out on a Thermo Neptune Plus® MC-ICP-MS installed at the Centro de Geociencias, Universidad Nacional Autonóma de México, in Juriquilla, Querétaro, on Faraday cups in static mode (González-Guzmán et al., 2016). The sample solutions were introduced to the plasma via an Aridus® desolvating sample introduction system using an Ar carrier gas and a blended Ar + N_2 sweep gas. The Hf fraction was taken up with 1 mL of 0.56 M HNO_3-0.24 M HF solution and the Lu fraction from 0.6 mL of 0.1 M HNO_3 solution. For Lu isotope data acquisition one block of 40 cycles with 4 seconds integration time each was performed. The ^{177}Hf intensity was measured to monitor for isobaric interference of ^{176}Hf on the ^{176}Lu signal. For the mass bias correction, each sample was doped with ~10 ppb of Re and the masses 185 and 187 were measured simultaneously. For Hf isotope data acquisition 8 blocks with 10 cycles per block and an integration time of 4 seconds per cycle were measured. Isobaric interferences of ^{176}Yb and ^{176}Lu on the ^{176}Hf signal were monitored by measuring ^{172}Yb and ^{175}Lu. Moreover, ^{181}Ta and ^{182}W were measured to monitor for isobaric interferences of ^{180}Ta and ^{180}W on the spiked isotope ^{180}Hf. To examine the accuracy of Hf isotope measurement, a 50 ppb JMC-475 Hf standard solution was measured after every 4-5 unknowns. The average $^{176}Hf/^{177}Hf$ ratio of JMC-475 measured over the last three years during a total of six analytical sessions is 0.282149 ± 0.000025 (n= 41). Data reduction was carried out using IsotopeHf®, an R-based data reduction software package that transforms raw mass spectrometry data into meaningful isotopic ratios, including all the necessary corrections for spiked samples (González-Guzmán et al., 2016).

Results

Five zircon grains from Permian plutonic rocks that had been dated by LA-ICP-MS have been chosen for isotope dilution MC-ICP-MS analyses. These include two zircons from the Orizaba-1 sample, two from the Paso de Ovejas-2 sample and one from the Linares-1 sample. The analyzed zircons are characterized by typical igneous textures (oscillatory and sector zoning), with no indication of inherited cores. However, all three samples do contain zircons, not used for Hf analysis, that display inherited cores (geochronology results section).

Paso de Ovejas-2 zircons yielded the lowest initial εHf values of -12.1 to -10.4, with corresponding two-step TDM(Hf) model ages of 1.9 and 1.82 Ga (Table. 4.). The Orizaba-1 sample has slightly higher εHf(t) of -9.3 and -6.0, with corresponding TDM(Hf) of 1.75 and 1.56 Ga (Table. 4). Differences observed in the Lu-Hf isotopic signatures between the two analyzed zircons from the Orizaba sample likely reflect heterogeneities in the source, as evidenced by the diverse populations of inherited zircons found in the sample (geochronology results section). Zircons from the Lineras-1 sample yielded the highest εHf(t) values of -4.6, with corresponding TDM(Hf) of 1.47 Ga (Table. 4).

DISCUSSION

I-Type vs. S-Type

The alumina saturation index (ASI) of Chappell and White (1974) distinguishes between metaluminous (I-type) and peraluminous (S-type) granitoids. The ASI values for the samples have been plotted against their U-Pb age in Fig. 8. The Early Permian (n= 3) and Late Permian-Early Triassic samples (n= 13) that display no zircon inheritance yield ASI values typical of I-type granitoids (0.73-1.01 and 0.45-1.08 respectively). The Late Permian-Early Triassic samples with inherited zircon cores yield higher ASI values (0.92-1.18), but are still mainly I-type. The higher ASI values in the samples with inherited zircon cores indicate a contribution from a more peraluminous (e.g. crustal sedimentary) source.

The ASI results indicate that the basement of the Western Gulf of Mexico is predominantly I-type (metaluminous) in composition, with minor S-type (peraluminous) influence. The observation that the more peraluminous samples preserve zircon cores, whereas the metaluminous samples do not, is consistent with the zircon solubility model of Watson and Harrison (1983) for I- and S-type magmas. It is unclear from the ASI values if the I-type granites are primary melts from juvenile mantle or if they are derived from the re-melting of pre-existing crustal igneous rocks.

Mantle Derived melts vs. Crustal Anatexis

Although there are only few samples analyzed, strongly negative εHf(t) values (-12 to -6) of the Late Permian-Early Triassic granitoids of the Western Gulf of Mexico are a significant result that indicates that the magmas from which the zircons crystallized were mainly formed by continental anatexis. TDM(Hf) model ages of these samples suggest that this crust was probably juvenile in the early Mesoproterozoic or late Palaeoproterozoic. The zircon analyzed from the Linares sample, yielding εHf(t) of -4.6 and TDM(Hf) of 1.47, is the only analysis that might include a slightly younger juvenile component. It is likely that the Late Permian-Early Triassic granitoids from this study formed through the fusion of Oaxaquia continental crust, as their Hf isotope evolution trend, expressed from TDM(Hf) model ages, is indistinguishable from those of Mesoproterozoic Oaxaquia into which they emplaced (Fig. 9; Weber et al., 2010; Weber et al., 2014).

However, it is important to highlight this conclusion is based on the Hf isotope analysis of only five zircon grains from a study area spanning several hundreds of kilometers. A more comprehensive Lu-Hf isotopic study of the basement along the Western Gulf of Mexico is needed to confirm this anatectic origin.

Late Permian-Early Triassic granitoids from the Sierra Pinta, Northern Mexico (Arvizu and Iriondo, 2011), Oaxaca (Ortega-Obregón et al., 2014), Colombia and Ecuador (Cochrane et al., 2014) have Lu-Hf isotope signatures that are similar to those reported here (Fig. 9). However, they also display evidence for mantle-crustal mixing, with some TDM(Hf) model ages that are younger than the Paleoproterozoic Laurentian crust (Sierra Pinta) and Mesoproterozoic Oaxaquia crust (Oaxaca) in which they emplaced.

Late Carboniferous-Early Permian granitoids of the Oaxaca area (Ortega-Obregón et al., 2014) show clear evidence for mantle-crust mixing and appear unrelated to the Late Permian-Early Triassic granitoids of the Western Gulf of Mexico (Fig. 9). Geochronological similarities, as well as spatial proximity of the Late Carboniferous-Early Permian granitoids of the Oaxaca area and Early Permian granitoids of the Western Gulf of Mexico suggest they may be analogous.

PETROGENESIS

The geochemistry of the granitoids from the Western Gulf of Mexico is similar to that of plutonic rocks of similar age intruding the Acatlán Complex (Kirsch, 2012), Oaxacan Complex (Ortega-Obregón et al., 2014) and Chiapas Massif (Weber et al., 2005). The probability density diagram of Fig. 10 suggests that Carboniferous-Triassic magmatism in Mexico was intermittent. The earliest phase of magmatism is clearly documented between 311-286 Ma, but inherited cores reported in this study indicate that this magmatism may have initiated in the Mississippian (ca. 326 Ma; Supplementary Material 1). A second and more prevalent phase of magmatism occurred between 274 and 243 Ma. This magmatism inherited zircons from the Late Carboniferous-Late Permian event, as well as from Oaxaquia (Grenville).

Jurassic reconstructions of Western Pangaea place Mexico close to the Laurussia-Gondwana suture (Pindell and Kennan, 2009). This, along with geochronological similarities with Carboniferous-Permian magmatism in the Variscan and Alleghanian orogenies and geochemical constraints presented in this study, suggests that the Permo-Triassic magmatism of Mexico is related to the final stages of the formation of Pangaea.

Late Carboniferous-Early Permian Arc

Trace element signatures of the Late Carboniferous-Early Permian granitoids from the Western Gulf of Mexico (this study) and Acatlán area (Kirsch, 2012) indicate that they formed in a continental arc setting. This interpretation is consistent with the Lu-Hf isotopic signatures for the Late Carboniferous-Early Permian granitoids of the Oaxaca area (Ortega-Obregón et al., 2014), which indicate mantle derived melts mixing with continental crust. This arc system intrudes into Oaxaquia continental crust, suggesting a Gondwanan affinity.

In Ortega-Obregón et al. (2014) this continental arc system is explained by the eastward dipping subduction of the Panthalassa Ocean beneath Pangaea. However, there is a strong correlation between the timing of the final amalgamation of Pangaea along the Ouachita-Marathon-Sonora suture ca. 290-280 Ma (Pindell and Dewey, 1982; Pindell, 1985; Ross, 1986; Viele and Thomas, 1989; Sedlock et al., 1993; Dickinson and Lawton, 2001) and the latest magmatism in the Late Carboniferous-Early Permian Arc (286 Ma; Ortega-Obregón et al., 2014). We therefore propose that the Late Carboniferous-Early Permian arc formed from the subduction of the Rheic Ocean on the margins of Gondwana, prior to the final amalgamation of Pangea (Fig. 11A&C). After the closure of the Rheic Ocean, and collision between Laurussia and Gondwana had occurred, the arc system shut down.

Late Permian-Early Triassic Post-Collisional Magmatism

The widespread Late Permian-Early Triassic granitoids of the Western Gulf of Mexico (this study), Oaxaca area (Ortega-Obregón et al., 2014) and Chiapas Massif (Weber et al., 2005; Estrada-Carmona et al., 2012) display trace element signatures that are consistent with formation in a continental arc environment. However, depleted Lu-Hf isotope signatures indicate the dominant process of magma generation was by crustal anatexis. This type of magmatism is more commonly associated with continental collision environments.

The Late Permian-Early Triassic granitoids of the Chiapas Massif, Western Gulf of Mexico and Oaxaca area postdate the final amalgamation of Pangaea (ca. 290-280 Ma) so are unlikely to represent a syn-collisional magmatic event. The granitoids may instead be associated with a phase of post-collisional magmatism (Fig. 11B&C), occurring during a period of thermal relaxation, after the final amalgamation of Pangaea, e.g., as seen in the Alleghanian orogeny ca. 300-275 Ma (Heatherington and Mueller, 2010; Mueller et al., 2014). Post-collisional granitoids of the Western Gulf of Mexico post-date equivalents in the Alleghanian orogeny by ca. 30 Ma. This lag period is consistent with the diachronic assembly of Pangaea, with Laurentia-Gondwana collision occurring in the Alleghanian orogeny ca. 335 Ma (Wortman et al., 1998) and along the Ouachita-Marathon-Sonora segment ca. 290 Ma (Pindell and Dewey, 1982; Pindell, 1985; Ross, 1986; Viele and Thomas, 1989; Sedlock et al., 1993; Dickinson and Lawton, 2001).

Granitoids that form in such post-collisional settings often inherit arc-like trace element signatures from previous subduction events (e.g. Pearce et al., 1984; Grimes et al., 2015). Therefore, the subduction-related trace element signatures observed in the Late Permian- Early Triassic granitoids of Chiapas Massif, Western Gulf of Mexico and Oaxaca area may well be inherited from the Late Carboniferous-Early Permian arc (discussed above), as well as Oaxaquia, which comprises the lower continental crust. This hypothesis is supported by the widespread Oaxaquia and Late Carboniferous-Early Permian zircon inheritance observed in the Late Permian-Early Triassic igneous event (this study).

Late Permian-Early Triassic Arc

Late Permian-Early Triassic granitoids found in the Sierra Pinta, Sonora, Northeast Mexico (Arvizu and Iriondo, 2009) and in Colombia and Ecuador (Cochrane et al., 2014) appear distinct from granitoids of comparable age in the Western Gulf of Mexico and Southern Mexico. The

TDM(Hf) model ages in the Sierra Pinta, Colombia and Ecuador display evidence for mantle-crustal mixing, which is more typical of continental arcs. We therefore agree with the interpretations of these authors that granitoids of Northeast Mexico, Colombia and Ecuador represent a Late Permian-Early Triassic arc, associated with the subduction of the Palaeo-Pacific beneath Pangaea (Fig. 11C).

Subsequent Tectonic Activity

In many models of Pangaea, overlap is observed between central and southern Mexico and northwest South America (Pindell and Dewey, 1982; Pindell, 1985; Handschy et al., 1987; Pindell and Kennan, 2001). Therefore, the terranes of central and Southern Mexico are likely to be allochthonous in origin. This implies that the terranes, into which the Carboniferous-Triassic plutons of the Oaxaca area, Chiapas Massif and Western Gulf of Mexico were intruded, migrated from elsewhere during the breakup of Pangaea.

Opening of the Gulf of Mexico

A possible mechanism for terrane migration occurred during the Early Jurassic in association with the early stages of the opening of the Gulf of Mexico, along the Mojave-Sonora Megashear (Anderson and Schmidt, 1983; Böhnel, 1999; Pindell and Kennan, 2001). This shear zone is proposed to have accommodated 700 km of left lateral motion along the southwestern flank of the North American Plate (Anderson and Schmidt, 1983; Pindell and Kennan, 2001; Pindell and Kennan, 2009). In this scenario the terranes of central and Southern Mexico (including the Acatlán Complex and Oaxacan Complex) originate in Northeast Mexico (Fig. 11D).

In plate reconstructions of Pangaea, the Yucatan block is positioned adjacent to Florida, and displaced to the south in a rotational motion during the main phase of the opening of the Gulf of Mexico in the Late Jurassic (Pindell and Dewey, 1982; Pindell, 1985; Schouten and Klitgord, 1994; Dickinson and Lawton, 2001; Jacques et al., 2004; Bird et al., 2005; Imbert, 2005; Imbert and Phillippe, 2005; Pindell et al, 2005). This movement likely affected the post-collisional granitoids of the Western Gulf of Mexico and Chiapas Massif, shearing the basement and displacing it to the south (Fig. 11E).

This tectonic activity associated with the breakup of Pangaea provides a mechanism for migration of the Late Carboniferous-Early Permian arc granitoids and Late Permian-Early Triassic post-collisional granitoids. The rocks were displaced to the south, away from the Laurentian-Gondwanan suture from which they originated (Fig. 11 D&E).

CONCLUSIONS

This contribution has shown that the crystalline basement of the Western Gulf of Mexico formed as a result of three distinct magmatic events, replacing and reworking pre-existing Oaxaquia continental crust on the margins of Gondwana. These magmatic events have been interpreted to be related to the following tectonic settings:

- An Early Permian (ca. 294 Ma) continental arc that formed in response to the subduction of the Rheic Ocean under the northern margins of Gondwana, prior to the final amalgamation of Pangaea. We propose that these Early Permian granitoids of the Western Gulf of Mexico are related to coeval Late Carboniferous-Early Permian granitoids that intrude the Acatlán Complex and Oaxaca area.
- Late Permian-Early Triassic (263-243 Ma) late- to post-collisional anatectic magmatism that formed from orogenic collapse in the Marathon-Sonora section of the Pangaea collision zone. We propose that they are coeval with Late Permian-Early Triassic granitoids of the Oaxaca area and Chiapas Massif.

- An Early Jurassic (188-164 Ma) continental arc, which is likely to be a part of the Nazas arc now exposed in northern Central Mexico.

These granitoids have been subsequently displaced from their original positions during the breakup of Pangaea. The initial phase of migration occurred in the Early Jurassic during the early phases of the opening of the Gulf of Mexico, which displaced Late Carboniferous-Early Permian and Late Permian-Early Triassic granitoids of the Acatlán and Oaxaca areas to the south along the Mojave-Sonora Megashear. Displacement of the Late Permian-Early Triassic granitoids of the Chiapas Massif and Western Gulf of Mexico occurred in the Late Jurassic, during the main phase of Gulf of Mexico opening as the Yucatan block rotated counterclockwise

ACKNOWLEDGMENTS

We would like to thank Juan Pablo Zapata, Ricardo Milián, Roberto Molina, Diego Villagómez, Maria Isabel Sierra Rojas, Rodrigo León and Kurt Wogau for their help during sample preparation. Additionally, a huge thank you must be extended to Uwe Martens for all of his help and guidance over the past few years. Finally, we would like to thank the reviewers for their constructive suggestions and comments.

REFERENCES CITED

Anderson, T. H. & Schmidt, V. A. 1983. The evolution of middle America and the Gulf of Mexico Caribbean Sea region during Mesozoic time. Geological Society of America Bulletin, 94, 941-966.

Andersen, T., 2002. Correction of common lead in U-Pb analyses that do not report 204Pb. Chemical Geology, 192, 59-79.

Arvizu, H. E. & Iriondo, A. 2011. Hf isotopic study of zircons from Permian granitoids of NW Mexico: Evidence for mixing of magmas derived from multiple crustal sources. Revista Mexicana De Ciencias Geologicas, 28, 493-518.

Barboza-Gudino, J. R., Orozco-Esquivel, M. T., Gomez-Anguiano, M. & Zavala-Monsivais, A. 2008. The early mesozoic volcanic arc of western North America in northeastern Mexico. Journal of South American Earth Sciences, 25, 49-63.

Bird, D. E., Burke, K., Hall, S. A. & Casey, J. F. 2005. Gulf of Mexico tectonic history: Hotspot tracks, crustal boundaries, and early salt distribution. AAPG Bulletin, 89, 311-328.

Bohnel, H. 1999. Paleomagnetic study of Jurassic and Cretaceous rocks from the Mixteca terrane (Mexico). Journal of South American Earth Sciences, 12, 545-556.

Bouvier, A., Vervoort, J. D. & Patchett, P. J. 2008. The Lu–Hf and Sm–Nd isotopic composition of CHUR: Constraints from unequilibrated chondrites and implications for the bulk composition of terrestrial planets. Earth and Planetary Science Letters, 273, 48-57.

Bussien, D., Bussy, F., Magna, T. & Masson, H. 2011. Timing of Palaeozoic magmatism in the Maggia and Sambuco nappes and paleogeographic implications (Central Lepontine Alps). Swiss Journal of Geosciences, 104, 1-29.

Bussy, F., Hernandez, J. & Von Raumer, J. 2000. Bimodal magmatism as a consequence of the post-collisional readjustment of the thickened Variscan continental lithosphere (Aiguilles Rouges–Mont Blanc Massifs, Western Alps). Geological Society of America Special Papers, 350, 221-233.

Chappell, B. W. & White, A. J. R. 1974. two contrasting granite types. Pacific Geology, 8, 173-174.

Cochrane, R., Spikings, R., Gerdes, A., Ulianov, A., Mora, A., Villagómez, D., Putlitz, B. & Chiaradia, M. 2014. Permo-Triassic anatexis, continental rifting and the disassembly of western Pangaea. Lithos, 190, 383-402.

Condie, K. C., Beyer, E., Belousova, E., Griffin, W. L. & O'Reilly, S. Y. 2005. U–Pb isotopic ages and Hf isotopic composition of single zircons: The search for juvenile Precambrian continental crust. Precambrian Research, 139, 42-100.

Dickinson, W. R. & Lawton, T. F. 2001. Carboniferous to Cretaceous assembly and fragmentation of Mexico. Geological Society of America Bulletin, 113, 1142-1160.

Ducea, M. N., Gehrels, G. E., Shoemaker, S., Ruiz, J. & Valencia, V. A. 2004. Geologic evolution of the Xolapa Complex, southern Mexico: Evidence from U-Pb zircon geochronology. Geological Society of America Bulletin, 116, 1016-1025.

Duncan Keppie, J., Nance, R. D., Dostal, J., Lee, J. K. W. & Ortega-Rivera, A. 2012. Constraints on the subduction erosion/extrusion cycle in the Paleozoic Acatlán Complex of southern Mexico: Geochemistry and geochronology of the type Piaxtla Suite. Gondwana Research, 21, 1050-1065.

Elías-Herrera, M., Ortega-Gutiérrez, F., Sánchez-Zavala, J. L., Macías-Romo, C., Ortega-Rivera, A. & Iriondo, A. 2005. La falla de Caltepec: Raíces expuestas de una frontera tectónica de larga vida entre dos terrenos continentales del sur de México. Boletín de la Sociedad Geológica Mexicana, 57, 83-109.

Estrada-Carmona, J., Weber, B., Martens, U. & Lopez-Martinez, M. 2012. Petrogenesis of Ordovician magmatic rocks in the southern Chiapas Massif Complex: relations with the early Palaeozoic magmatic belts of northwestern Gondwana. International Geology Review, 54, 1918-1943.

Godinez-Urban, A., Lawton, T. F., Molina Garza, R. S., Iriondo, A., Weber, B. & Lopez-Martinez, M. 2011. Jurassic volcanic and sedimentary rocks of the La Silla and Todos Santos Formations, Chiapas: Record of Nazas arc magmatism and rift-basin formation prior to opening of the Gulf of Mexico. Geosphere, 7, 121-144.

González-Guzmán, G., Weber, B., Tazzo-Rangel, M. T., Solari, L.A. 2016. Validation of digestion and element separation methods and a new data reduction program (IsotopeHf®) for Lu-Hf isotope dilution analysis by MC-ICP-MS. Revista Mexicana de Ciencias Geológicas. 33, 254-269.

Griffin, W. L., Wang, X., Jackson, S. E., Pearson, N. J., O'Reilly, S. Y., Xu, X. & Zhou, X. 2002. Zircon chemistry and magma mixing, SE China: In-situ analysis of Hf isotopes, Tonglu and Pingtan igneous complexes. Lithos, 61, 237-269.

Grimes, C. B., Wooden, J. L., Cheadle, M. J. & John, B. E. 2015. "Fingerprinting" tectono-magmatic provenance using trace elements in igneous zircon. Contributions to Mineralogy and Petrology, 170.

Handschy, J. W., Keller, G. R. & Smith, K. J. 1987. The Ouachita system in Northern Mexico. Tectonics, 6, 323-330.

Heatherington, A. L., Mueller, P. A. & Wooden, J. L. 2010. Alleghanian plutonism in the Suwannee terrane, USA: Implications for late Paleozoic tectonic models. Geological Society of America Memoirs, 206, 607-620.

Imbert, P. 2005. The Mesozoic opening of the Gulf of Mexico: Part 1, Evidence for oceanic accretion during and after salt deposition. Transactions of the 25th Annual GCSSEPM Research Conference: Petroleum systems of divergent continental margins, 1119-1150.

Imbert, P. & Phillippe, Y. 2005. The Mesozoic opening of the Gulf of Mexico: Part 2, Integrating seismic and magnetic data into a general opening model. Transactions of the 25th Annual GCSSEPM Research Conference: Petroleum systems of divergent continental margins, 1151-1189.

Jackson, S. E., Pearson, N. J., Griffin, W. L. & Belousova, E. A. 2004. The application of laser ablation-inductively coupled plasma-mass spectrometry to in situ U-Pb zircon geochronology. Chemical Geology, 211, 47-69.

Jacques, J.M., Price, A.D. & Bain, J.E. 2004. Digital integration of potential fields and geologic data sets for Plate tectonic and basin dynamic modeling -the first step toward identifying new play concepts in the Gulf of Mexico Basin. The Leading Edge, 23, 384-389.

Keppie, D. J., Dostal, J., Murphy, B. J. & Nance, D. 2008. Synthesis and tectonic interpretation of the westernmost Paleozoic Variscan orogen in southern Mexico: From rifted Rheic margin to active Pacific margin. Tectonophysics, 461, 277-290.

Keppie, J. D. 2004. Terranes of Mexico revisited: A 1.3 billion year odyssey. International Geology Review, 46, 765-794.

Keppie, J. D., Dostal, J., Cameron, K. L., Solari, L. A., Ortega-Gutierrez, F. & Lopez, R. 2003. Geochronology and geochemistry of Grenvillian igneous suites in the northern Oaxacan Complex, southern Mexico: tectonic implications. Precambrian Research, 120, 365-389.

Keppie, J. D., Dostal, J., Ortega-Gutierrez, F. & Lopez, R. 2001. A Grenvillian arc on the margin of Amazonia: evidence from the southern Oaxacan Complex, southern Mexico. Precambrian Research, 112, 165-181.

Kirsch, M. 2012. Continental arc development along the periphery of Pangea: Late Paleozoic pluton emplacement and basin evolution in a transtensional setting, eastern Acatlán Complex, Mexico. PhD Thesis. Universidad Nacional Autónoma de México.

Kirsch, M., Keppie, J. D., Murphy, J. B. & Solari, L. A. 2012. Permian–Carboniferous arc magmatism and basin evolution along the western margin of Pangea: Geochemical and geochronological evidence from the eastern Acatlán Complex, southern Mexico. Geological Society of America Bulletin, 124, 1607-1628.

Lawlor, P. J., Ortega-Gutiérrez, F., Cameron, K. L., Ochoa-Camarillo, H., Lopez, R. & Sampson, D. E. 1999. U-Pb geochronology, geochemistry, and provenance of the Grenvillian Huiznopala Gneiss of Eastern Mexico. Precambrian Research, 94, 73-99.

Lawton, T. F. & Molina Garza, R. S. 2014. U-Pb geochronology of the type Nazas Formation and superjacent strata, northeastern Durango, Mexico: Implications of a Jurassic age for continental-arc magmatism in north-central Mexico. Geological Society of America Bulletin, 126, 1181-1199.

Le Maitre, R. W., et al. 1989. A classification of igneous rocks and glossary of terms Blackwell, Oxford.

Loomis, J., Weaver, B. & Blatt, H. 1994. Geochemistry of Mississippian tuffs from the Ouachita Mountains, and implications for the tectonics of the Ouachita orogen, Oklahoma and Arkansas. Geological Society of America Bulletin, 106, 1158-1171.

Lopez-Ramos, E. 1979. Geología de México, Edición privada.

Ludwig, K. R. 2012. User's manual for Isoplot 3.75; A geochronological toolkit for Microsoft Excel. Berkeley Geochronology Center Special Publication 5, 1-75.

Mcdonald, I. & Viljoen, K. S. 2006. Platinum-group element geochemistry of mantle eclogites: a reconnaissance study of xenoliths from the Orapa kimberlite, Botswana. Applied Earth Science, 115, 81-93.

Mcdonough, W. F. & Sun, S. S. 1995. The composition of the Earth. Chemical Geology, 120, 223-253.

Mueller, P. A., Heatherington, A. L., Foster, D. A., Thomas, W. A. & Wooden, J. L. 2014. The Suwannee suture: Significance for Gondwana-Laurentia terrane transfer and formation of Pangaea. Gondwana Research, 26, 365-373.

Nebel-Jacobsen, Y., Scherer, E.E., Münker, C., Mezger, K. 2005. Separation of U, Pb, Lu, and Hf from single zircons for combined U–Pb dating and Hf isotope measurements by TIMS and MC-ICPMS. Chemical Geology, 220, 105-120.

Ortega-Gutierrez, F., Elias-Herrera, M., Moran-Zenteno, D. J., Solari, L., Luna-Gonzalez, L. & Schaaf, P. 2014. A review of batholiths and other plutonic intrusions of Mexico. Gondwana Research, 26, 834-868.

Ortega-Gutierrez, F., Ruiz, J. & Centeno-Garcia, E. 1995. Oaxaquia, a Proterozoic microcontinent accreted to North America during the late Paleozoic. Geology, 23, 1127-1130.

Ortega-Obregón, C., Duncan Keppie, J., Murphy, J. B., Lee, J. K. W. & Ortega-Rivera, A. 2009. Geology and geochronology of Paleozoic rocks in western Acatlán Complex, southern Mexico: Evidence for contiguity across an extruded high-pressure belt and constraints on Paleozoic reconstructions. Geological Society of America Bulletin, 121, 1678-1694.

Ortega-Obregón, C., Solari, L., Gomez-Tuena, A., Elias-Herrera, M., Ortega-Gutiérrez, F. & Macias-Romo, C. 2014. Permian-Carboniferous arc magmatism in southern Mexico: U-Pb dating, trace element and Hf isotopic evidence on zircons of earliest subduction beneath the western margin of Gondwana. International Journal of Earth Sciences, 103, 1287-1300.

Pearce, J. A., Harris, N. B. W. & Tindle, A. G. 1984. Trace-element discrimination diagrams for the tectonic interpretation of granitic-rocks. Journal of Petrology, 25, 956-983.

Pindell, J. & Dewey, J. F. 1982. Permo-Triassic reconstruction of Western Pangea and the evolution of the Gulf of Mexico Caribbean region. Tectonics, 1, 179-211.

Pindell, J. & Kennan, L. 2001. Kinematic Evolution of the Gulf of Mexico and Caribbean. GCSSEPM Foundation 21st Annual Research Conference Transactions. Petroleum Systems of Deep-Water Basins, 193-220.

Pindell, J., Kennan, L., Maresch, W. V., Stanek, K. P., Draper, G. & Higgs, R. 2005. Plate-kinematics and crustal dynamics of circumCaribbean arc-continent interactions, and tectonic controls on basin development in Proto-Caribbean margins. Caribbean–South American Plateinteractions, Venezuela. Geological Society of America, Special Paper, 394, 7-52.

Pindell, J. L. 1985. Alleghenian reconstruction and subsequent evolution of the Gulf of Mexico, Bahamas, and Proto-Caribbean. Tectonics, 4, 1-39.

Pindell, J. L. & Kennan, L. 2009. Tectonic evolution of the Gulf of Mexico, Caribbean and northern South America in the mantle reference frame: an update. Origin and Evolution of the Caribbean Plate, 328, 1-55.

Poole, F. G., Perry, W. J., Madrid, R. J. & Amaya-Martinez, R. 2005. Tectonic synthesis of the Ouachita-Marathon-Sonora orogenic margin of southern Laurentia: Stratigraphic and structural implications for timing of deformational events and plate-tectonics model Geological Society of America Special Paper, 293, 543-596.

Von Raumer, J.F. & Bussy, F. 2004. Mont Blanc and Aiguilles Rouges Geology of their polymetamorphic basement (external massifs, France - Switzerland), Lausanne, Université de Lausanne, Section des Sciences de la Terre.

Ross, C. A. 1986. Paleozoic evolution of southern margin of Permian basin. Geological Society of America Bulletin, 97, 536–554.

Ratschbacher, L., Franz, L., Min, M.., Bachmann, R., Martens, U., Stanek, K., Stübner K., Nelson, B.K., Herrmann, U., Weber, B., López-Martínez, M., Jonckheere, R., Sperner, B., Tichomirowa, Marion, Mcwilliams, M.O., Gordon, M., Meschede, M., Bock, P. 2009. The North American-Caribbean Plate boundary in Mexico-Guatemala-Honduras

Schaltegger, U. 1997. Magma pulses in the Central Variscan Belt: episodic melt generation and emplacement during lithospheric thinning. Terra Nova, 9, 242-245.

Schouten, H. & Klitgord, K. D. 1994. Mechanistic solutions to the opening of the Gulf of Mexico. Geology, 22, 507-510.

Schulze, C. 2011. Petrología y geoquímica de las rocas del área de Pluma Hidalgo, Oaxaca e implicaciones tectónicas para el Proterozoico de Oaxaquia. Universidad Autónoma Nacional de México, México, PhD thesis, 311 pp.

Sedlock, R. L., Ortega-Gutiérrez, F. & Speed, R. C. 1993. Tectonostratigraphic terranes and tectonic evolution of Mexico. Geological Society of America Special Paper, 293.

Shaulis, B. J., Lapen, T. J., Casey, J. F. & Reid, D. R. 2012. Timing and Rates of Flysch Sedimentation In the Stanley Group, Ouachita Mountains, Oklahoma and Arkansas, U.S.A.: Constraints from U-Pb Zircon Ages of Subaqueous Ash-Flow Tuffs. Journal of Sedimentary Research, 82, 833-840.

Sláma, J., Kosler, J., Condon, D., Crowley, J., Gerdes, A., Hanchar, J., Horstwood, M., Morris, G., Nasdala, L., Norberg, N., Schaltagger, U., Schoene, B., Tubrett, M.N., and Whitehouse, M.J., 2008. Plešovice zircon—A new natural reference material for U-Pb and Hf isotopic microanalysis. Chemical Geology, 249, 1-35.

Solari, L. A., Keppie, J. D., Ortega-Gutiérrez, F., Cameron, K. L., Lopez, R. & Hames, W. E. 2003. 990 and 1100 Ma Grenvillian tectonothermal events in the northern Oaxacan Complex, southern Mexico: roots of an orogen. Tectonophysics, 365, 257-282.

Solari, L. A., Gómez-Tuena, A., Bernal, J. P., Pérez-Arvizu, O., and Tanner, M., 2010. U-Pb Zircon Geochronology with an Integrated LA-ICP-MS Microanalytical Workstation: Achievements in Precision and Accuracy. Geostandards and Geoanalytical Research, 34, 5-18.

Solari, L. A. & Tanner, M. 2011. UPb.age, a fast data reduction script for LA-ICP-MS U-Pb geochronology. Revista Mexicana de Ciencias Geológicas, 28, 83-91.

Spikings, R., Cochrane, R., Villagómez, D., Van Der Lelij, R., Vallejo, C., Winkler, W. & Beate, B. 2015. The geological history of northwestern South America: from Pangaea to the early collision of the Caribbean Large Igneous Province (290-75 Ma). Gondwana Research, 27, 95-139.

Sun, S.-S. & Mcdonough, W. F. 1989. Chemical and isotopic systematics of oceanic basalts: implications for mantle composition and processes. Geological Society, London, Special Publications, 42, 313-345.

Talavera-Mendoza, O., Ruiz, J., Gehrels, G. E., Meza-Figueroa, D. M., Vega-Granillo, R. & Campa-Uranga, M. F. 2005. U-Pb geochronology of the Acatlán Complex and implications for the Paleozoic paleogeography and tectonic evolution of southern Mexico. Earth and Planetary Science Letters, 235, 682-699.

Van Der Lelij, R., Spikings, R., Ulianov, A., Chiaradia, M. & Mora, A. 2016. Palaeozoic to Early Jurassic history of the northwestern corner of Gondwana, and implications for the evolution of the Iapetus, Rheic and Pacific Oceans. Gondwana Research, 31, 271-294.

Vega-Granillo, R., Calmus, T., Meza-Figueroa, D., Ruiz, J., Talavera-Mendoza, O. & Lopez-Martinez, M. 2009. Structural and tectonic evolution of the Acatlán Complex, southern Mexico: Its role in the collisional history of Laurentia and Gondwana. Tectonics, 28.

Vega-Granillo, R., Talavera-Mendoza, O., Meza-Figueroa, D., Ruiz, J., Gehrels, G. E., Lopez-Martinez, M. & De La Cruz-Vargas, J. C. 2007. Pressure-temperature-time evolution of Paleozoic high-pressure rocks of the Acatlán Complex (southern Mexico): Implications for the evolution of the Iapetus and Rheic Oceans. Geological Society of America Bulletin, 119, 1249-1264.

Vervoort, J. D., Patchett, P. J., Albarede, F., Blichert-Toft, J., Rudnick, R. & Downes, H. 2000. Hf-Nd isotopic evolution of the lower crust. Earth and Planetary Science Letters, 181, 115-129.

Viele, G. W. & Thomas, W. A. 1989. Tectonic synthesis of the Ouachita orogenic belt. In: In Hatcher, R. D., Jr., Et Al., Eds (ed.) The Appalachian-Ouachita orogenic belt in the United States: Boulder, Colorado, Geological Society of America, Geology of North America.

Vinasco, C. J., Cordani, U. G., Gonzalez, H., Weber, M. & Pelaez, C. 2006. Geochronological, isotopic, and geochemical data from Permo-Triassic granitic gneisses and granitoids of the Colombian Central Andes. Journal of South American Earth Sciences, 21, 355-371.

Walsh, G. J., Aleinikoff, J. N. & Wintsch, R. P. 2007. Origin of the Lyme Dome and implications for the timing of multiple Alleghanian deformational and intrusive events in southern Connecticut. American Journal of Science, 307, 168-215.

Watson, E. B. & Harrison, T. M. 1983. Zircon saturation revisited- temperature and composition effects in a variety of crustal magma types. Earth and Planetary Science Letters, 64, 295-304.

Weber, B., Cameron, K. L., Osorio, M. & Schaaf, P. 2005. A late Permian tectonothermal event in Grenville crust of the southern Maya terrane: U-Pb zircon ages from the Chiapas massif, southeastern Mexico. International Geology Review, 47, 509-529.

Weber, B., Iriondo, A., Premo, W. R., Hecht, L. & Schaaf, P. 2007. New insights into the history and origin of the southern Maya block, SE Mexico: U-Pb-SHRIMP zircon geochronology from metamorphic rocks of the Chiapas massif. International Journal of Earth Sciences, 96, 253-269.

Weber, B., Scherer, E. E., Schulze, C., Valencia, V. A., Montecinos, P., Mezger, K. & Ruiz, J. 2010. U-Pb and Lu-Hf isotope systematics of lower crust from central-southern Mexico - Geodynamic significance of Oaxaquia in a Rodinia Realm. Precambrian Research, 182, 149-162.

Weber, B. & Schulze, C. H. 2014. Early Mesoproterozoic (> 1.4 Ga) ages from granulite basement inliers of SE Mexico and their implications on the Oaxaquia concept - Evidence from U-Pb and Lu-Hf isotopes on zircon. Revista Mexicana De Ciencias Geologicas, 31, 377-394.

Wilson, M. 1989. Igneous Petrogenesis, Springer Netherlands.

FIGURE CAPTIONS

Figure 1. (A) schematic map of Mexico displaying the extent of Oaxaquia type basement. Carboniferous-Triassic pluton exposures in Mexico are also displayed (Elías-Herrera., 2005; Weber et al., 2005; Ratschbacher et al., 2009; Arvizu and Iriondo, 2011; Kirsch et al., 2012; Ortega-Obregón et al., 2007 and 2014). (B) location of wells from which basement sample were taken in this study.

Figure 2. Photomicrographs of the analyzed samples. Abbreviations are as follows: Chl- chlorite, Cpx- clinopyroxene, Ttn- titanite, Qtz- quartz, Zrn- zircon, Pl- plagioclase, Ser- sericite, Prg- pargasite, Phl- phlogopite, Ol- olivine, Id- iddingsite, Bt- biotite, Am- amphibole, Cal- calcite, Ep- epidote. A) Hydrothermally altered granite containing quartz, plagioclase (partially seriticized), chlorite, titanite and zircon as a minor phase; XPL. B) hydrothermally altered granite with abundant secondary calcite; XPL. C) Granodiorite containing quartz, plagioclase, biotite and amphibole; XPL. D) Hydrothermally altered granite with epidote; XPL. E) Mafic porphyry containing olivine, iddingsite and plagioclase phenocrysts and a matrix of feldspars; XPL. F) Micro diorite containing partially chloritized biotite and minor clinopyroxene.

Figure 3. Tera-Wasserburg, Wetherill and weighted mean diagrams for the dated samples along the Western Gulf of Mexico. Th/U vs. age plots are also included, as well as U vs. age plots where metamictization is suspected.

Figure 4. Cathodoluminescence images of the zircons in each of the analyzed samples. M= metamictization; Hf= zircons used for Lu-Hf isotope analysis (dilution method). We were unable to determine the appropriate ages for the corresponding laser spots in some of the samples, due to an error during data collection.

Figure 5. Classification diagrams for the basement core samples of the Western Gulf of Mexico. A) Quartz-Alkali feldspar-Plagioclase-Feldspathoid (QAPF) diagram. CIPW norms first calculated then Q, A, P, F percentages recalculated to 100%. 1= quartzolite, 2= quartz-rich granitoids, 3= alkali feldspar granite, 4= granite (a-syeno-granite, b- monzo-granite), 5= granodiorite, 6= tonalite, 7= quartz diorite/ quartz gabbro/ quartz anorthosite, 8= quartz monzodiorite/ quartz monzogabbro, 9= quartz monzonite, 10= quartz syenite, 11= quartz alkali feldspar syenite, 12= alkali feldspar syenite, 13= syenite, 14= monzonite, 15= monzodiorite/ monzogabbro, 16= diorite/ gabbro/ anorthosite. B) Total alkali-silica (TAS) diagram of Le Maitre et al., (1989). Field boundaries taken from Wilson (1989).

Figure 6. (A) chondrite normalized REE and (B) N-MORB normalized multi-element plot for the basement samples from the Western Gulf of Mexico. Chondrite normalizing values are taken from Sun and McDonough (1989) and N-MORB normalizing values are taken from McDonough and Sun (1995).

Figure 7. Ta-Yb, Nb-Y, Rb-(Y+Nb) and Rb-(Yb+Ta) tectonic discrimination diagrams (Pearce et al., 1984). P-T Chiapas= Permo-Triassic Chiapas (Weber et al., 2005; Estrada-Carmona et al.,

2012); P-T Colombia= Permo-Triassic Colombia (Vinasco et al., 2006; Cochrane et al., 2014); Totoltepec Pluton, Cozahuico Granite and La Carbonera Stock (Kirsch, 2012).

Figure 8. Alumina saturation index (ASI) vs. age for the basement cores of the Western Gulf of Mexico.

Figure 9. εHf (t) vs. age plot for Western Gulf of Mexico samples selected for Hf isotope analysis on zircons (TIMS). Our results have been compared to other LA-ICP-MS data from around Mexico, Colombia and Ecuador. Intercept between εHf (t) and the depleted mantle curve based on a $^{176}Lu/^{177}Hf$ average crustal ratio of 0.015 (Griffin et al., 2002). Values for CHUR are from Bouvier et al., (2008). The fields represent zircon TDM(Hf) model ages from Permo-Triassic granitoids in Mexico, Ecuador and Colombia as well as for older igneous events such as the Paleoproterozoic Sierra Pinta and Oaxaquia continental crust.

Figure 10. Probability density plot for Carboniferous-Triassic granitoids from this study, Chiapas Massif, Sierra Pinta, Acatlán and Oaxaca areas.

Figure 11. (A) Late Carboniferous and (B) Permo-Triassic tectonic models for the formation of the granitoids along the Western Gulf of Mexico. (C) schematic palaeogeographic reconstruction of the western flank of the Pangaea collision zone. The green stars represent magmatism related to a continental arc in Sonora (Laurentian side) and Colombia (Gondwanan side). (D) and (E) represent phases of shearing in the Permo-Triassic anatectic province.

TABLE 1: PREVIOUS GEOCHRONOLOGY

Area	Age (Ma)	Method	Reference
Western Gulf Of Mexico	312-916	K-Ar	Lopez-Ramos, 1979
Sosola rhyolite	270.5 ± 2.5	U/Pb zircon	Ortega-Obregón et al., 2014
Cuanana pluton	310.8 ± 1.8	U/Pb zircon	Ortega-Obregón et al., 2014
Carbonera stock	272.5 ± 1.0	U/Pb zircon	Ortega-Obregón et al., 2014
Zaniza batholith	287.0 ± 1.9	U/Pb zircon	Ortega-Obregón et al., 2014
Etla granite	255.2 ± 1.0	U/Pb zircon	Ortega-Obregón et al., 2014
Honduras batholith	290.1 ± 2.2	U/Pb zircon	Ortega-Obregón et al., 2014
Xolapa Complex	272.0 ± 10	U/Pb zircon	Ducea et al., 2004
Chiapas Massif	251-258	U/Pb zircon	Weber et al., 2005
Chiapas Massif	271.9 ± 2.7	U/Pb zircon	Weber et al., 2007
Cozahuico granite	270.4 ± 2.6	U/Pb zircon	Elías-Herrera et al., 2005
Sierra Pinta granites	265-275	U/Pb zircon	Arvizu and Iriondo, 2011
Toltoltepec pluton	306.0 ± 1.0	U/Pb zircon	Kirsch et al., 2012
Toltoltepec pluton	289.0 ± 1.0	U/Pb zircon	Kirsch et al., 2012
Toltoltepec pluton	289 ± 1	U/Pb zircon	Keppie et al., 2004
Toltoltepec pluton	287 ± 1	U/Pb zircon	Yañez et al., 1991
Chichihualtepec dike	265-275	U/Pb zircon	Kirsch et al., 2012
Rabinal complex	215-270	U/Pb zircon	Ratschbacher et al., 2009

Henry Coombs; Table 1; Manuscript 1

TABLE 2: GEOCHRONOLOGY OF THIS STUDY

Sample	Age (Ma)
Early Permian	
Pinonal *(1)*	294.1 ± 3.4
Arenque	293.5 ± 3.7
Paso de Oro	274.2 ± 3.5
Late Permian-Early Triassic	
Cupelado	262.7 ± 4.5
Orizaba	261.1 ± 4.9
Plan de Las Hayas *(1)*	261.0 ± 3.9
Nayade	257.0 ± 5.2
Paso de Ovejas	256.7 ± 5.5
Trincheras	254.6 ± 3.4
Linares	255.1 ± 4.8
Erizo	249.8 ± 2.7
Plan de Las Hayas *(2)*	251.7 ± 5.2
Pinonal *(2)*	249.8 ± 3.2
Tamaulipas	247.9 ± 4.0
Benemerito	245.4 ± 4.6
Chaneque	243.4 ± 2.8
Jurassic	
Muro	188.3 ± 4.0
Tlapacoyan	163.5 ± 4.7

Henry Coombs; Table 2; Manuscript 1

TABLE 3: MAJOR AND TRACE ELEMENT GEOCHEMISTRY

Sample	Plan de las Hayas *(1)*	Arenque	Paso de Oro	Benemerito	Trincheras	Pinonal *(1)*	Linares	Paso de Ovejas
Latitude	19°46'15.60"N	24°57'2.07"N	24°43'14.62"N	25°40'45.91"N	24°57'2.07"N	25°40'45.91"N	24°43'14.62"N	19°15'33.17"N
Longitude	96°37'18.83"W	99°26'29.23"W	99°22'23.28"W	99°51'43.91"W	99°26'29.23"W	99°51'43.91"W	99°22'23.28"W	96°24'54.03"W
Major elements (wt%)								
SiO_2	62.73	66.94	65.05	71.01	68.78	56.03	67.02	67.19
TiO_2	0.78	0.47	0.52	0.21	0.50	0.90	0.19	0.54
Al_2O_3	16.10	15.04	16.06	14.40	15.66	13.43	11.82	15.32
Fe_2O_3	5.60	3.68	4.71	1.52	3.62	7.38	2.27	3.98
MnO	0.08	0.04	0.06	0.04	0.06	0.08	0.03	0.03
MgO	2.36	1.01	2.03	0.66	1.07	4.11	0.80	1.61
CaO	2.58	2.65	4.07	1.09	1.92	4.31	9.35	2.07
Na_2O	4.53	3.87	2.95	3.62	3.77	3.47	3.02	3.21
K_2O	2.54	5.63	3.43	5.64	3.28	4.43	3.90	4.61
P_2O_5	0.21	0.12	0.10	0.08	0.20	0.10	0.07	0.15
LOI	3.54	1.77	2.28	1.43	1.48	6.84	1.98	2.36
Total	101.05	101.22	101.25	99.69	100.32	101.07	100.45	101.09
Trace elements (ppm)								
V	106.16	86.26	101.49	24.01	46.84	207.32	23.07	71.52
Rb	51.75	99.90	74.64	212.68	130.98	90.17	93.35	78.75
Sr	688.34	337.77	314.68	312.93	383.62	138.89	337.55	404.50
Y	15.06	18.64	20.99	11.55	19.732	12.62	20.60	10.69
Zr	165.91	145.67	83.25	83.70	50.98	151.93	89.96	130.09
Nb	6.36	8.76	5.73	7.52	11.73	2.93	1.93	8.85
Cs	5.34	4.78	3.26	6.89	13.14	3.53	1.01	1.86
Ba	414.91	923.83	775.31	1539.42	1048.80	315.81	486.60	739.97
La	18.58	23.05	14.933	19.51	43.28	7.73	15.70	18.58
Ce	37.84	44.92	0.09	39.56	83.40	16.43	30.84	41.26
Pr	4.95	5.28	4.05	4.78	9.71	2.04	4.09	5.07
Nd	19.82	18.76	15.88	16.67	34.67	8.01	15.52	18.71
Sm	4.04	3.61	3.65	3.36	6.11	2.01	3.30	3.54
Eu	1.12	1.05	1.21	0.82	1.66	0.67	0.93	0.99
Gd	3.78	3.39	3.56	2.70	5.22	2.14	3.21	2.92
Tb	0.48	0.48	0.55	0.35	0.65	0.36	0.47	0.38
Dy	2.66	2.85	3.49	1.87	3.32	2.32	3.01	1.95
Ho	0.46	0.56	0.67	0.32	0.60	0.46	0.60	0.34
Er	1.40	1.79	2.04	0.98	1.83	1.42	1.99	1.06
Tm	0.20	0.29	0.32	0.16	0.28	0.24	0.31	0.16
Yb	1.34	1.90	2.07	1.06	1.75	1.57	2.05	1.12
Lu	0.20	0.33	0.33	0.18	0.30	0.26	0.32	0.18
Hf	4.36	4.33	2.34	2.71	6.81	4.37	2.60	3.59
Ta	0.53	0.85	0.47	0.48	0.99	0.26	0.17	0.74
Pb	4.59	7.70	8.82	48.14	21.09	4.36	12.57	8.74
Th	2.92	4.95	3.95	15.80	14.99	2.91	5.01	2.56
U	1.38	2.14	1.31	5.18	3.60	0.83	1.38	0.72

Sample	Chaneque	Erizo	Nayade	Tamaulipas	Cupelado	Plan de las Hayas *(2)*	Orizaba	Muro
Latitude	24°34'19.97"N	22°10'12.03"N	22°45'16.58"N	22°24'31.66"N	20°18'43.29"N	19°46'15.60"N	18°46'17.46"N	20°50'38.52"N
Longitude	98°38'2.21"W	97°31'6.47"W	97°36'14.99"W	97°57'13.29"W	97° 2'0.53"W	96°37'18.83"W	97° 4'43.88"W	97°26'46.19"W
Major elements (wt%)								
SiO_2	51.44	74.43	70.93	69.69	67.34	61.54	72.91	56.13
TiO_2	1.36	0.24	0.33	0.49	0.31	0.68	0.12	0.77
Al_2O_3	16.72	11.88	13.31	15.08	14.21	14.28	13.46	18.17
Fe_2O_3	8.88	0.77	2.71	3.29	2.47	4.43	1.26	7.76
MnO	0.08	0.03	0.04	0.05	0.04	0.07	0.02	0.11
MgO	4.15	0.12	0.37	1.26	0.74	1.81	0.24	3.53
CaO	3.21	2.43	2.09	3.07	2.85	4.60	1.12	6.55
Na_2O	3.37	2.11	2.26	4.09	3.62	5.31	3.88	3.25
K_2O	5.59	5.08	4.67	1.91	3.99	2.48	4.76	1.54
P_2O_5	0.29	0.04	0.12	0.12	0.10	0.20	0.03	0.14
LOI	6.28	3.63	3.58	0.60	3.47	5.42	1.01	2.64
Total	101.36	100.76	100.40	99.64	99.13	100.81	98.81	100.59

Sample	Chaneque	Erizo	Nayade	Tamaulipas	Cupelado	Plan de las Hayas *(2)*	Orizaba	Muro
Latitude	24°34'19.97"N	22°10'12.03"N	22°45'16.58"N	22°24'31.66"N	20°18'43.29"N	19°46'15.60"N	18°46'17.46"N	20°50'38.52"N
Longitude	98°38'2.21"W	97°31'6.47"W	97°36'14.99"W	97°57'13.29"W	97° 2'0.53"W	96°37'18.83"W	97° 4'43.88"W	97°26'46.19"W
Trace elements (ppm)								
V	205.18	24.79	33.68	54.59	13.24	68.30	16.79	173.27
Rb	137.92	133.06	88.36	55.80	89.96	53.29	109.39	17.83
Sr	419.40	115.32	314.02	470.37	303.09	183.47	288.25	382.21
Y	10.90	15.48	9.43	13.42	10.72	14.38	6.93	17.42
Zr	150.16	117.75	129.03	166.74	135.72	206.38	90.81	113.22
Nb	6.18	9.90	7.82	9.62	6.19	8.31	7.26	3.92
Cs	15.69	6.97	5.11	0.89	12.20	3.76	1.62	0.64
Ba	1125.66	1468.05	1081.40	1586.14	863.20	334.76	522.18	459.26
La	21.31	24.28	7.81	51.23	22.18	25.88	9.34	9.76
Ce	43.32	47.55	14.90	99.77	40.56	54.42	20.05	21.49
Pr	5.66	5.44	1.74	11.91	5.16	7.24	2.48	2.93
Nd	21.51	18.04	6.23	41.84	19.34	28.28	8.89	12.23
Sm	4.08	3.19	1.46	6.21	3.49	5.35	1.69	2.86
Eu	1.39	0.89	0.73	1.75	1.17	1.45	0.59	1.00
Gd	3.46	2.99	1.51	4.76	3.10	4.52	1.45	2.90
Tb	0.43	0.39	0.24	0.50	0.36	0.52	0.18	0.45
Dy	2.23	2.16	1.45	2.36	1.80	2.56	1.08	2.80
Ho	0.35	0.42	0.29	0.40	0.30	0.43	0.19	0.52
Er	0.95	1.35	0.90	1.23	0.91	1.18	0.63	1.64
Tm	0.13	0.24	0.16	0.19	0.13	0.17	0.12	0.27
Yb	0.72	1.64	1.05	1.15	0.84	1.05	0.82	1.71
Lu	0.11	0.28	0.19	0.19	0.13	0.17	0.16	0.28
Hf	3.68	3.77	3.54	4.27	3.39	5.25	2.98	2.89
Ta	0.38	0.88	0.74	0.54	0.53	0.70	0.55	0.24
Pb	7.31	54.86	13.66	13.64	11.62	5.26	11.71	5.62
Th	7.16	11.51	7.49	9.81	3.46	4.66	3.14	1.11
U	2.70	1.67	1.75	2.19	0.59	1.59	0.91	0.31

Sample	Tlapocoyan	Magdalena	Benemerito	Jurel	Trincheras	Standards		
Latitude	19°59'49.64"N	20°23'40.72"N	25°40'45.91"N	22° 9'4.42"N	24°57'2.07"N	NIM-G official	NIM-G measured	r.s.d.
Longitude	97° 8'47.80"W	97° 4'19.43"W	99°51'43.91"W	97°38'16.60"W	99°26'29.23"W			
Major elements (wt%)								
SiO_2	61.34	47.17	69.55	51.52	69.73	75.70	75.75	0.04
TiO_2	0.44	1.66	0.51	0.84	0.44	0.09	0.10	6.71
Al_2O_3	16.23	13.02	14.50	18.73	14.82	12.08	12.27	1.08
Fe_2O_3	2.50	8.36	2.09	4.79	3.37	2.02	2.04	0.77
MnO	0.05	0.12	0.05	0.15	0.07	0.02	0.02	4.07
MgO	0.94	7.72	0.82	4.25	1.00	0.06	0.02	73.24
CaO	4.03	9.65	1.24	5.70	1.89	0.78	0.76	1.82
Na_2O	4.90	1.81	3.67	3.94	3.41	3.36	3.25	2.33
K_2O	6.13	6.29	5.26	2.16	3.73	4.99	5.03	0.50
P_2O_5	0.23	1.48	0.11	0.38	0.18	0.01	0.01	0.62
LOI	3.99	4.17	1.40	6.59	1.95			
Total	100.79	101.45	99.21	99.05	100.57			
Trace elements (ppm)								
V	53.14	183.21	58.79	138.64	47.89	2.00	0.03	137.65
Rb	175.35	80.69	45.67	36.85	160.76	320.00	326.27	1.37
Sr	617.70	1551.75	348.02	759.47	354.30	10.00	7.52	20.01
Y	14.83	35.73	10.10	31.82	17.12	143.00	145.26	1.11
Zr	114.27	142.29	245.90	256.75	191.07	300.00	279.51	5.00
Nb	10.24	30.01	4.71	11.64	10.09	53.00	48.08	6.88
Cs	6.92	10.62	1.33	1.73	11.33	N.D.	0.87	10.06
Ba	1084.14	5427.39	544.82	1175.15	1531.09	120.00	105.82	8.88
La	25.23	242.04	15.78	36.32	43.13	109.00	111.73	1.75
Ce	50.10	491.43	31.25	79.89	82.87	195.00	200.55	1.98
Pr	6.03	61.06	3.76	10.25	9.54	N.D.	N.D.	N.D.
Nd	21.20	222.73	13.31	39.12	32.96	72.00	71.05	0.94
Sm	4.15	33.95	2.43	7.44	5.56	15.80	14.49	6.14
Eu	0.83	8.82	0.98	2.12	1.51	0.35	0.33	4.55
Gd	3.27	24.15	2.21	7.05	4.81	14.00	14.99	4.83

Henry Coombs; Table 3; Manuscript 1

Sample	Tlapocoyan	Magdalena	Benemerito	Jurel	Trincheras	Standards		
Latitude	19°59'49.64"N	20°23'40.72"N	25°40'45.91"N	22° 9'4.42"N	24°57'2.07"N	NIM-G official	NIM-G measured	r.s.d.
Longitude	97° 8'47.80"W	97° 4'19.43"W	99°51'43.91"W	97°38'16.60"W	99°26'29.23"W			
Tb	0.43	2.13	0.29	0.95	0.57	3.00	2.54	11.63
Dy	2.30	7.85	1.62	5.27	3.04	17.00	17.94	3.80
Ho	0.40	1.10	0.30	0.99	0.53	N.D.	N.D.	N.D.
Er	1.23	3.07	0.89	3.05	1.62	N.D.	N.D.	N.D.
Tm	0.21	0.33	0.15	0.48	0.25	2.00	2.15	5.15
Yb	1.37	1.96	0.99	2.92	1.51	14.20	14.04	0.79
Lu	0.23	0.29	0.17	0.49	0.26	2.00	2.09	3.19
Hf	3.79	2.81	5.66	6.36	5.13	12.00	11.57	2.56
Ta	0.75	2.36	0.31	0.80	0.97	4.50	4.07	7.16
Pb	38.30	45.54	8.45	17.74	17.70	40.00	30.87	18.21
Th	14.04	23.64	1.92	3.64	11.90	50.00	47.93	2.99
U	3.95	5.59	1.02	0.97	3.50	15.00	15.86	3.93

Henry Coombs; Table 3; Manuscript 1

TABLE 4: Lu-Hf DATA FOR ZIRCONS

Sample number	Lu-Hf isotopic ratios							age corrected (b)		Model Age(c)
	Lu (ppm)	Hf (ppm)	$^{176}Lu/^{177}Hf$	$^{176}Hf/^{177}Hf$	±2 s.e. ×10^6 ($2\sigma_m$)	ε Hf (a)	age (Ma)	$^{176}Hf/^{177}Hf$ (t)	ε Hf (t)	$TDM_{(Hf)}$ (Ga)
Orizaba										
N6F1C1-6	87	9257	0.001342	0.282449	5	-11.4	278	0.282442	-6.0	1.56
N6F1C1-35	57	6876	0.001181	0.282361	7	-14.5	267	0.282355	-9.3	1.75
Linares										
N7F1C1-6	41	11651	0.000500	0.282497	11	-9.7	253	0.282495	-4.6	1.47
Paso de Ovejas										
N6F9C2-11	23	8359	0.000398	0.282334	8	-15.5	254	0.282332	-10.4	1.82
N6F9C2-4	85	8701	0.001384	0.282295	5	-16.9	247	0.282288	-12.1	1.90

(a) Epsilon Hf is the deviation of $^{176}Hf/^{177}Hf$ of the sample relative to the chondritic uniform reservoir (CHUR) ×10^4. For the calculations present-day CHUR values $^{176}Hf/^{177}Hf_{CHUR(0)}$= 0.282785 and $^{176}Lu/^{177}Hf_{CHUR}$= 0.0336 (Bouvier et al., 2008)
(b) $^{176}Hf/^{177}Hf$ (t) and εHf(t) were calculated using the $^{206}Pb/^{238}U$ age of the zircons.
(c) Two-stage crustal residence model ages were calculated from the following equations:
$t_{DM}=(1/\lambda)\ln(1+m)$
$m= \{(^{176}Hf/^{177}Hf)_{DM}-[(^{176}Hf/^{177}Hf)_{i,zirc}+(^{176}Lu/^{177}Hf)_{avg.crust}(e^{\lambda t}-1)]\} / \{(^{176}Lu/^{177}Hf)_{DM}- (^{176}Lu^{177}Hf)_{avg.\ crust}\}$
Assumptions made: $(^{176}Lu/^{177}Hf)_{avg.crust}$= 0.015 (Condie et al.,2005)
Present day depleted mantle model is based on $(^{176}Hf/^{177}Hf)_{DM}$= 0.283224 (Vervoort et al., 2000) and $(^{176}Lu/^{177}Hf)_{DM}$= 0.03826 (Weber et al., 2010)

Henry Coombs; Table 4; Manuscript 1

Henry Coombs; Figure 1; Manuscript 1

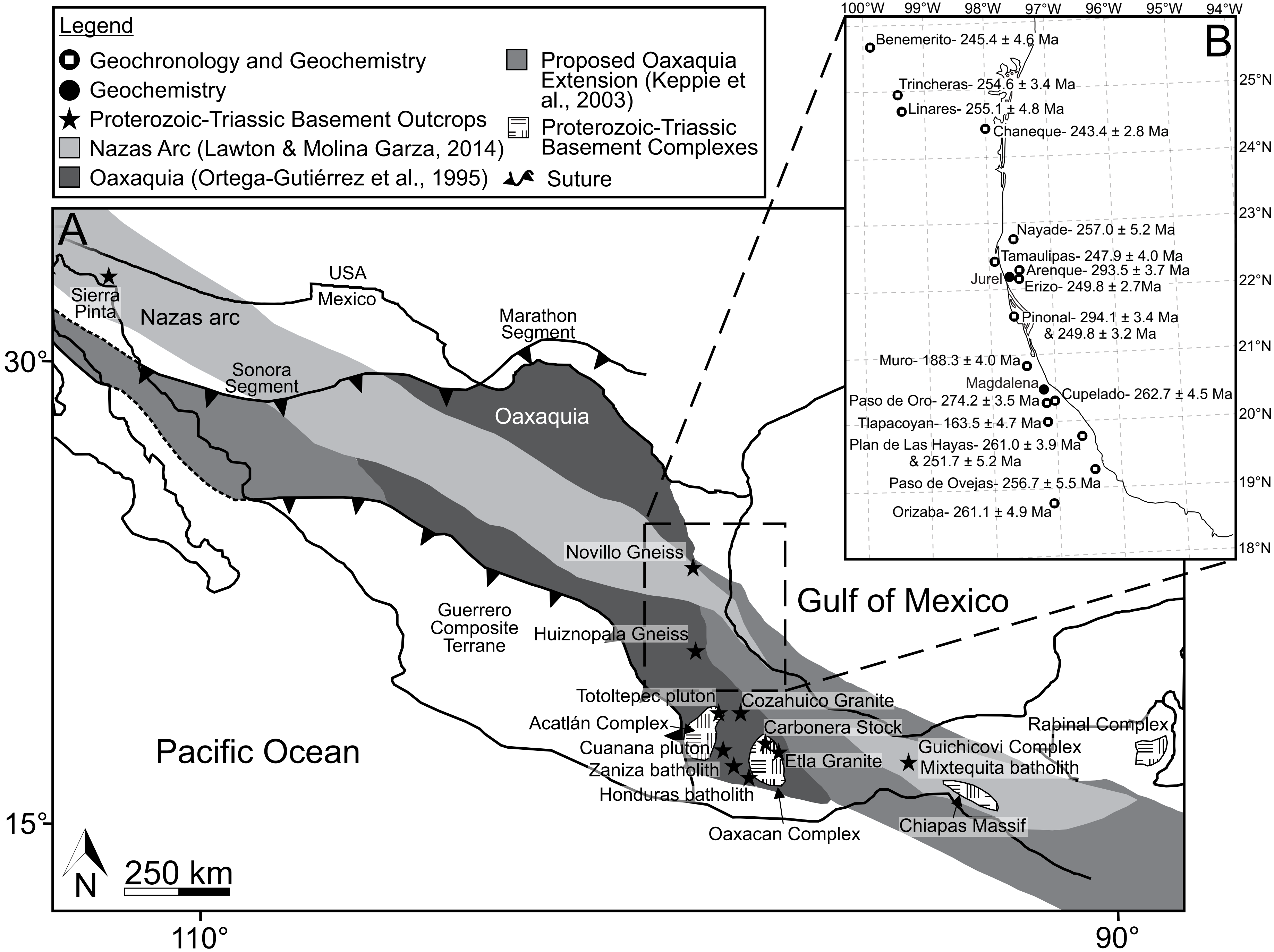

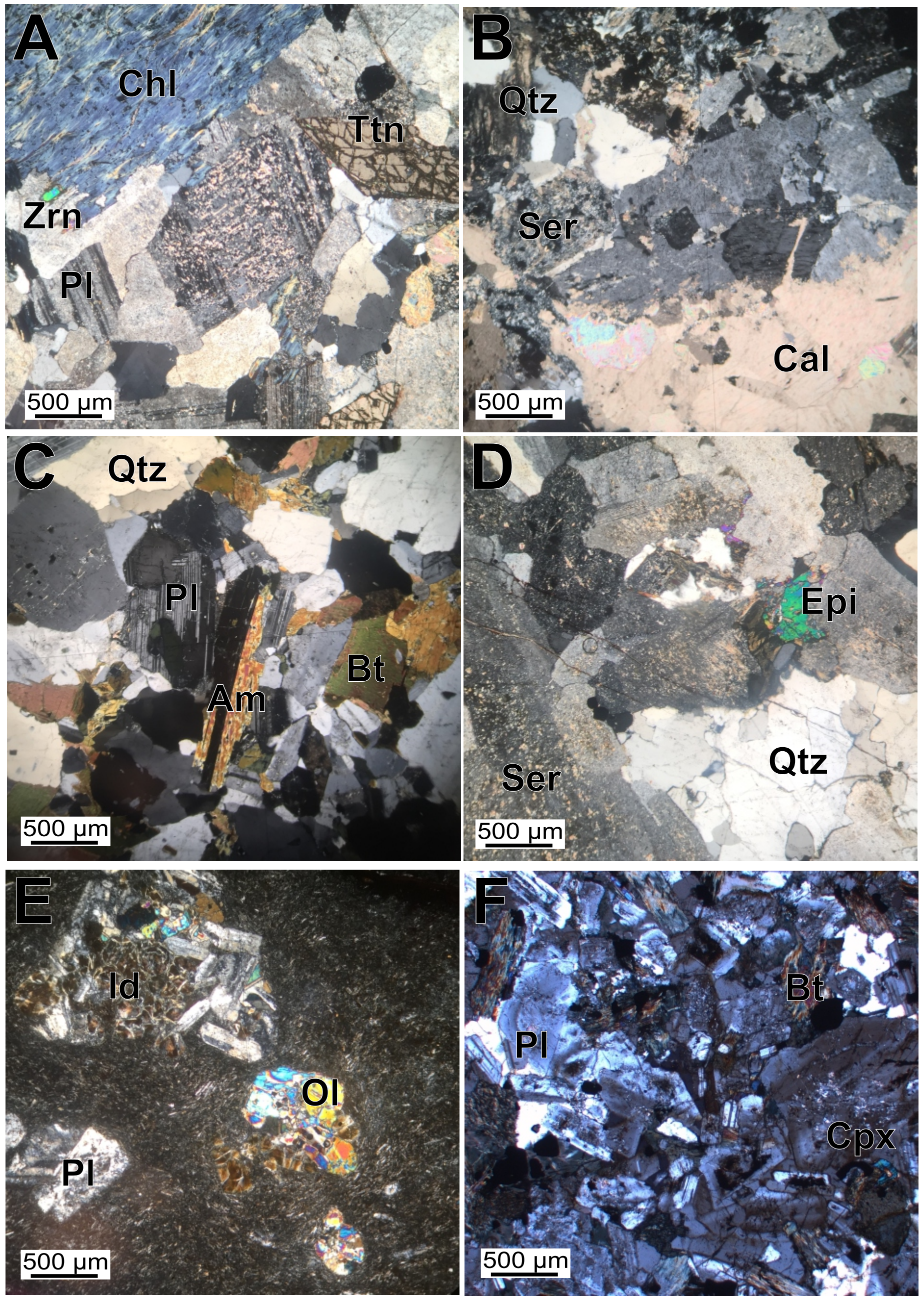

Henry Coombs; Figure 2; Manuscript 1

Henry Coombs; Figure 3; Manuscript 1

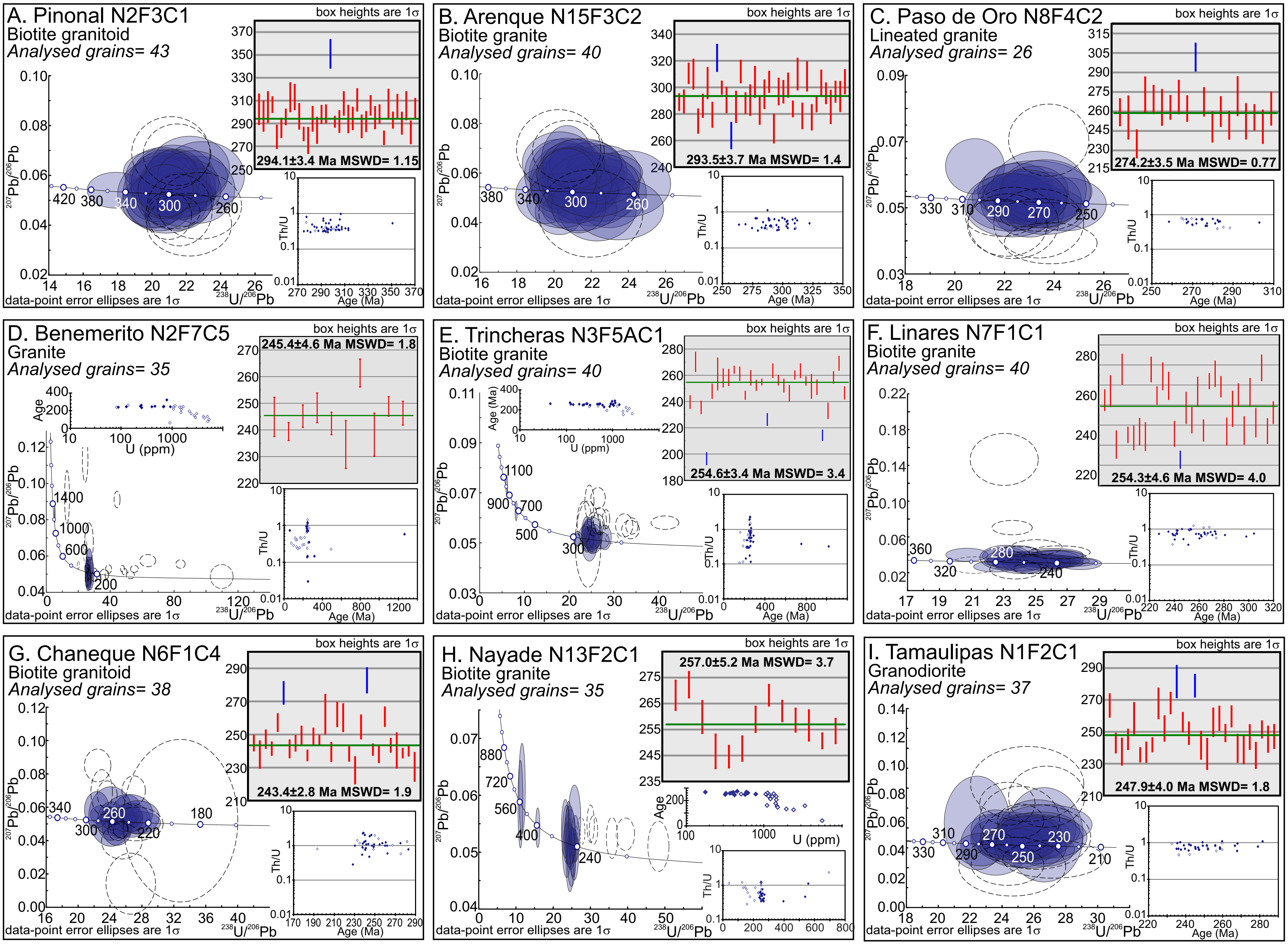

Henry Coombs; Figure 3; Manuscript 1

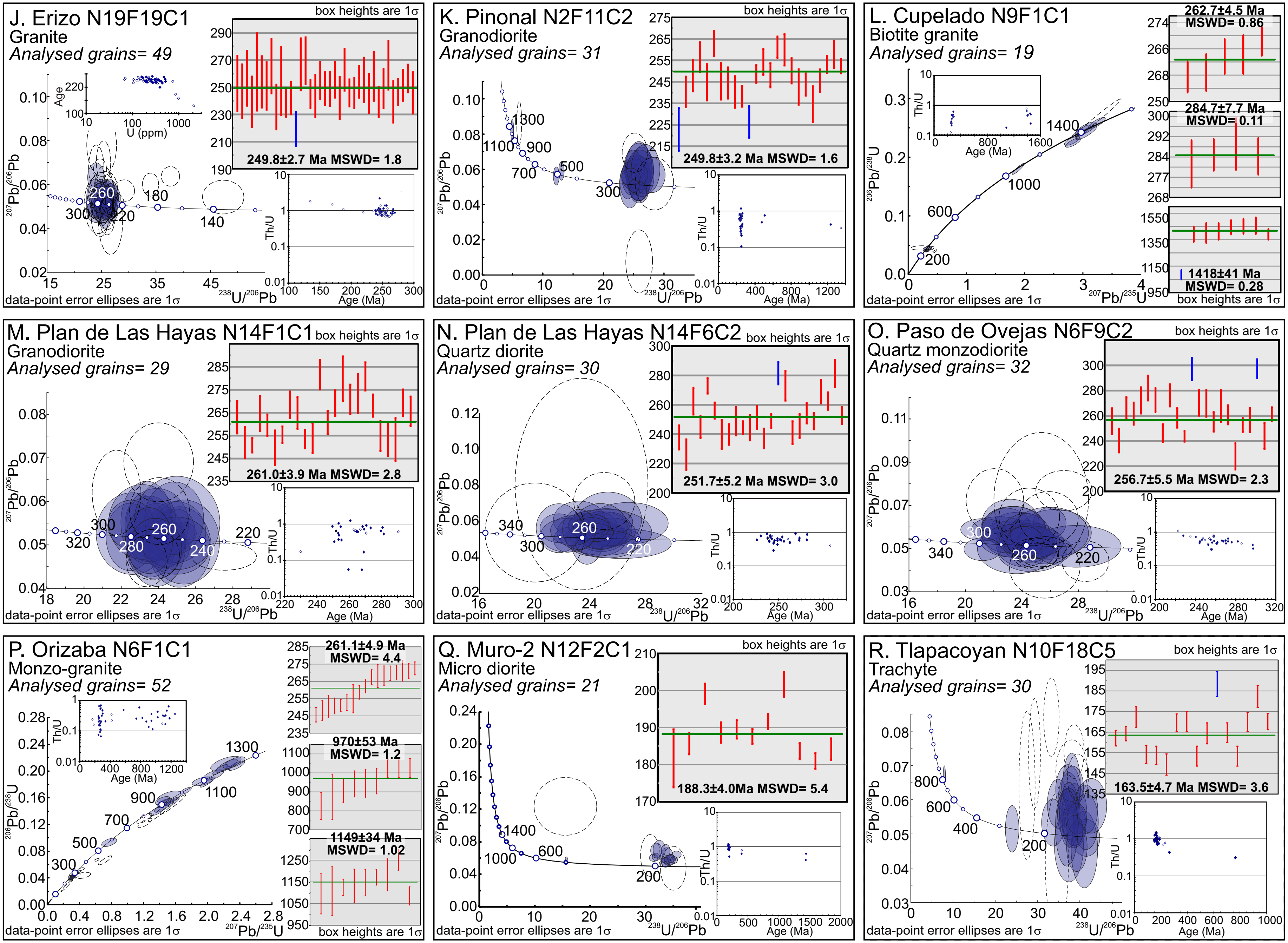

Henry Coombs; Figure 4; Manuscript 1

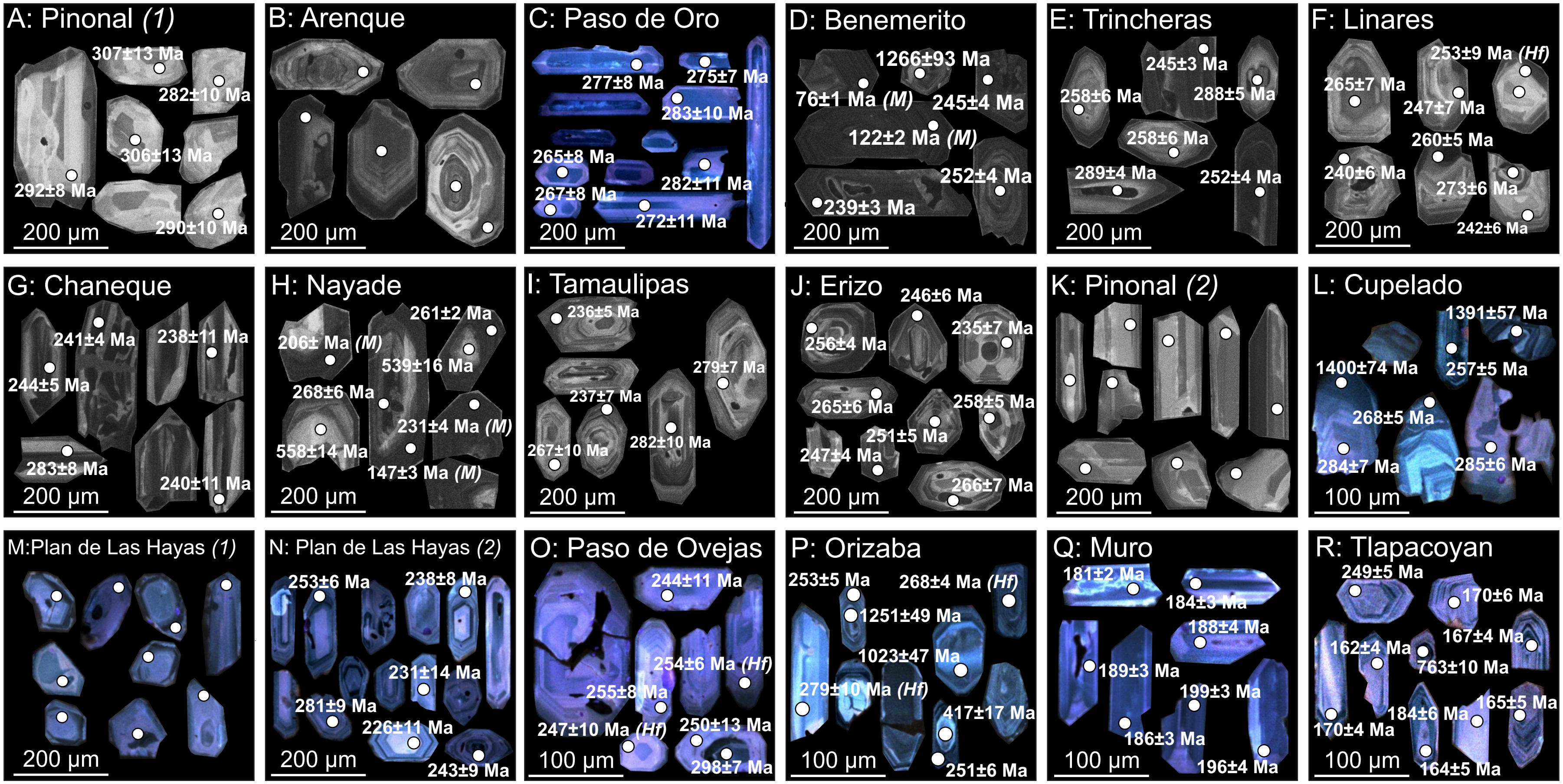

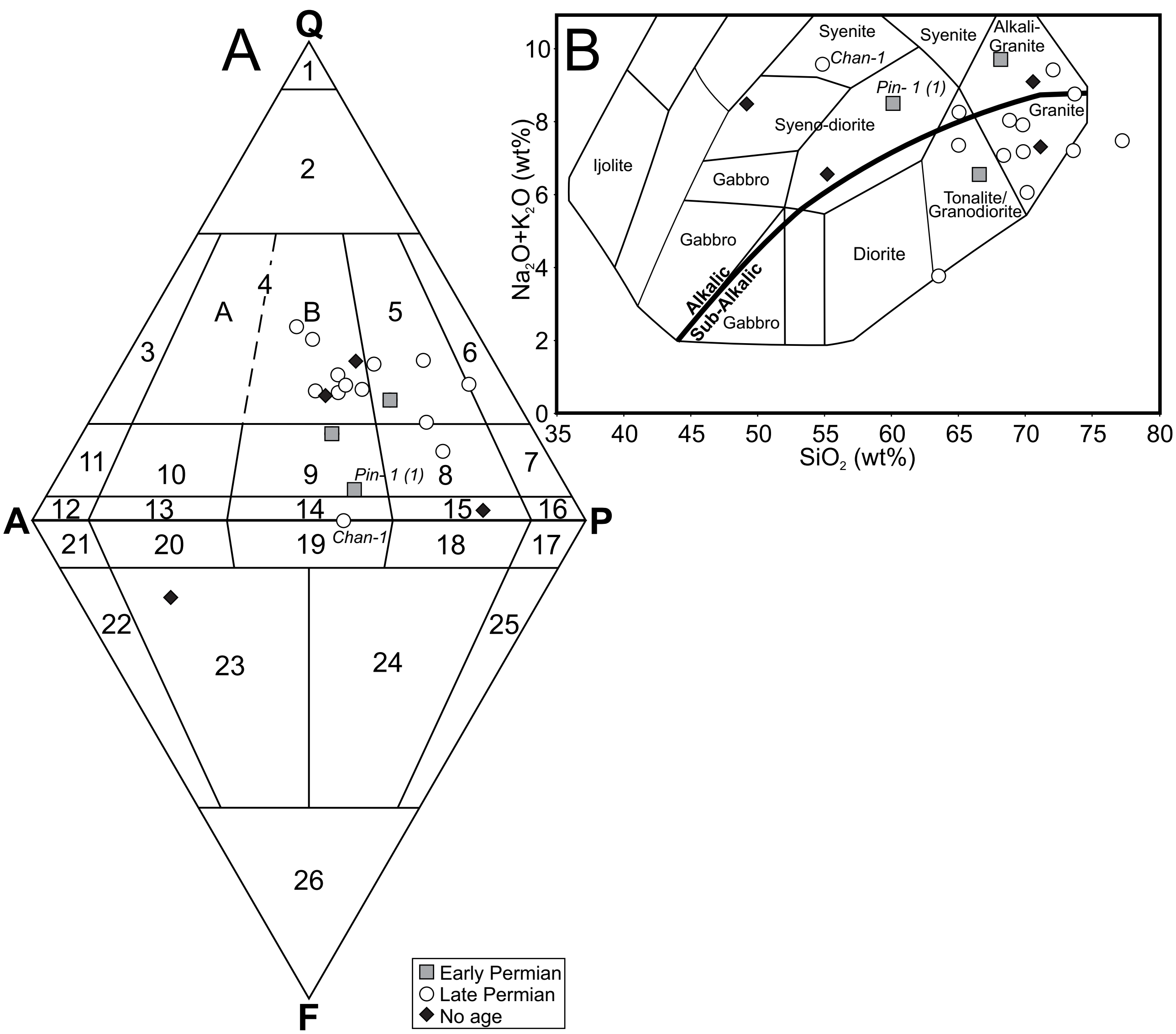

Henry Coombs; Figure 5; Manuscript 1

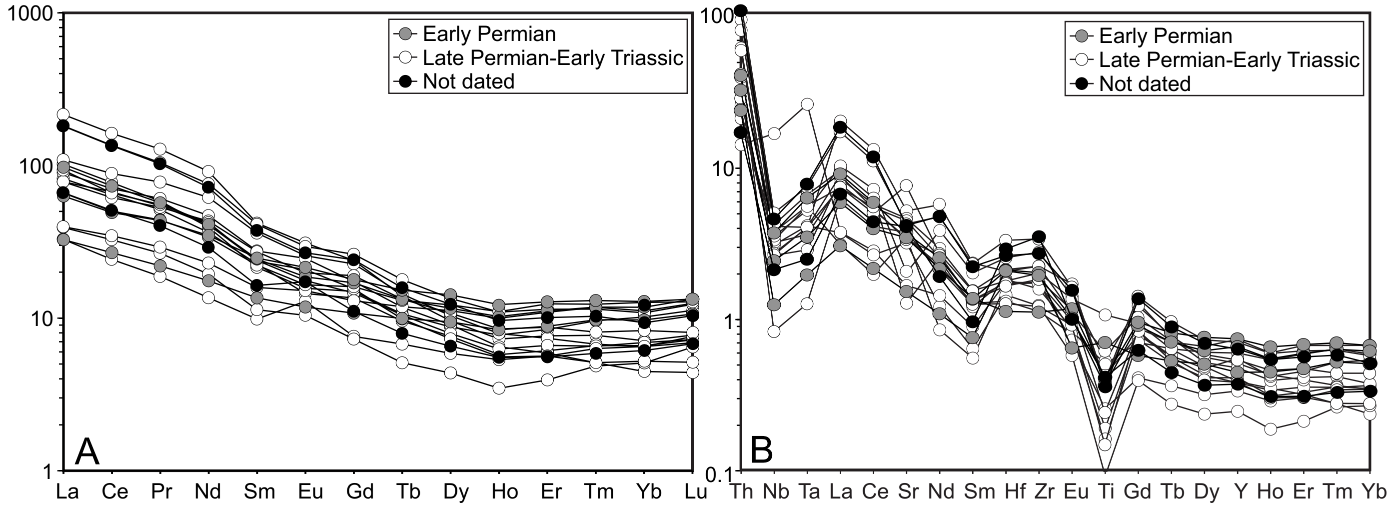

Henry Coombs; Figure 6; Manuscript 1

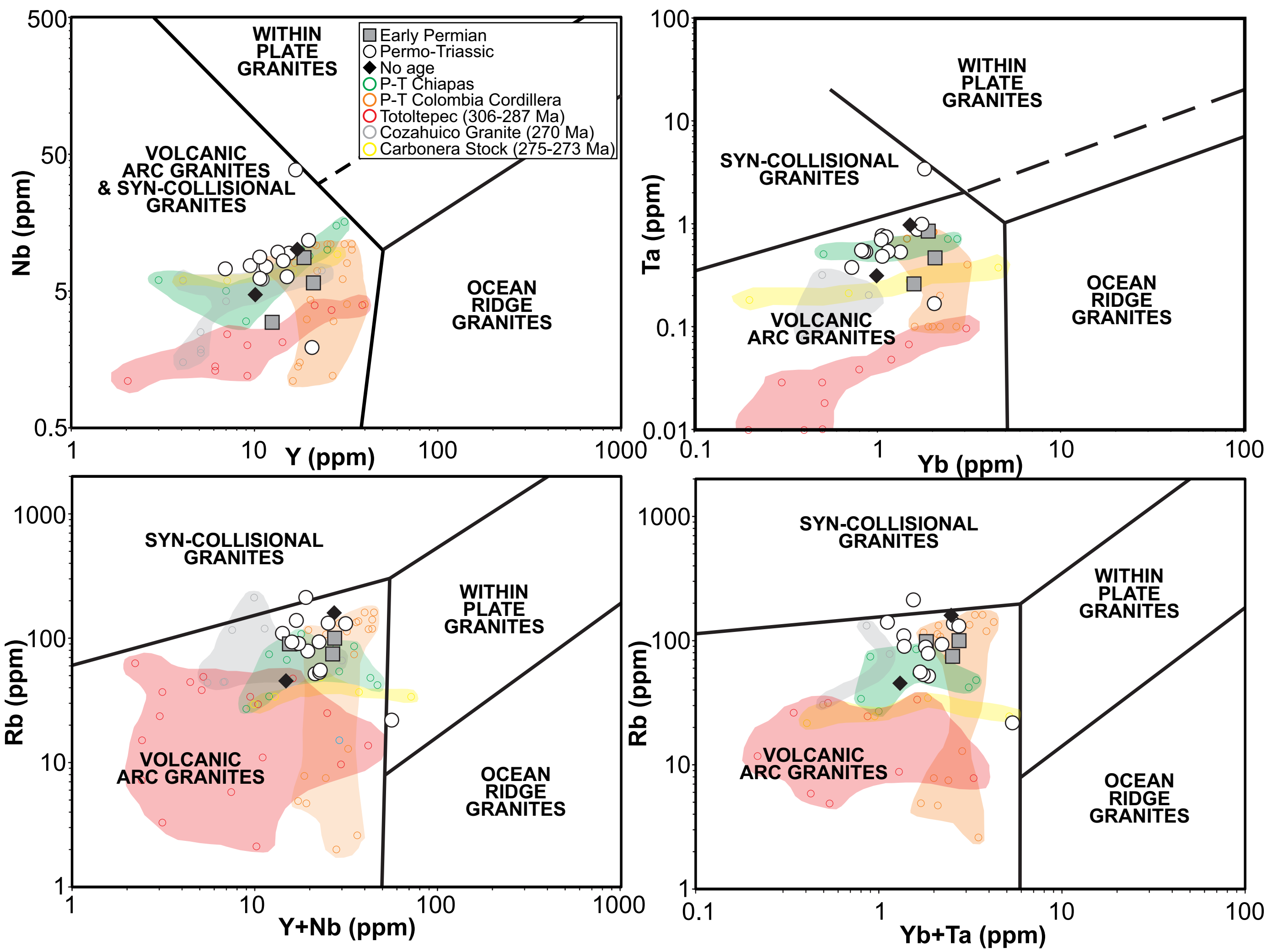

Henry Coombs; Figure 7; Manuscript 1

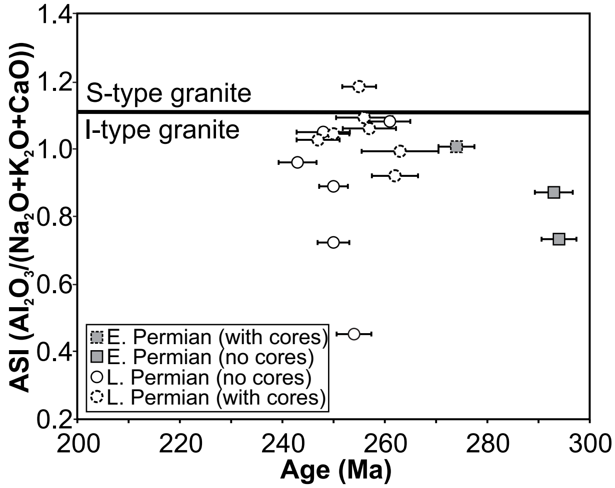

Henry Coombs; Figure 8; Manuscript 1

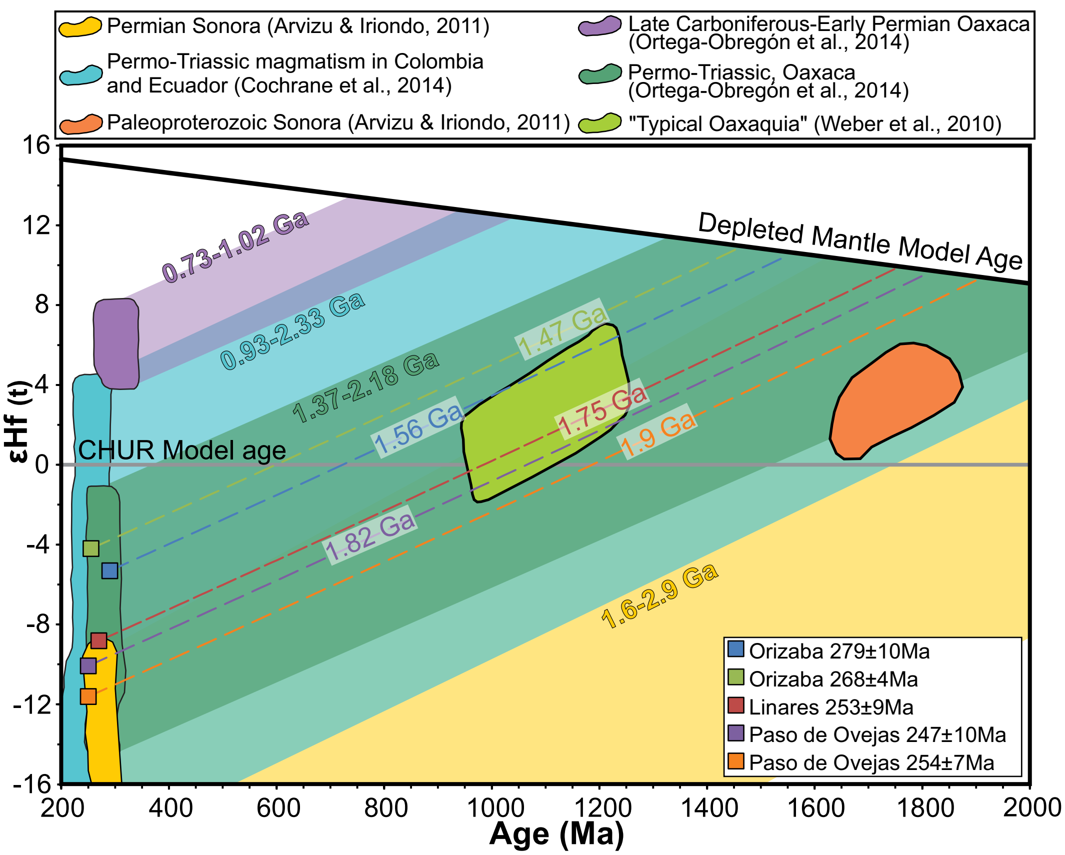

Henry Coombs; Figure 9; Manuscript 1

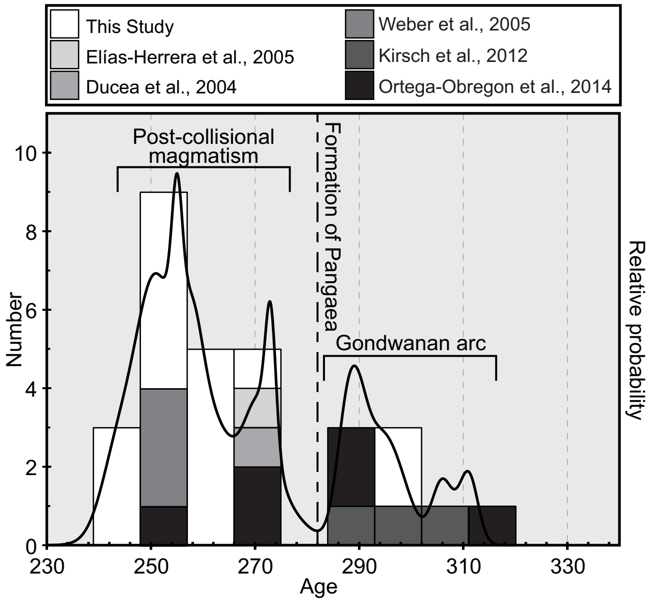

Henry Coombs; Figure 10; Manuscript 1

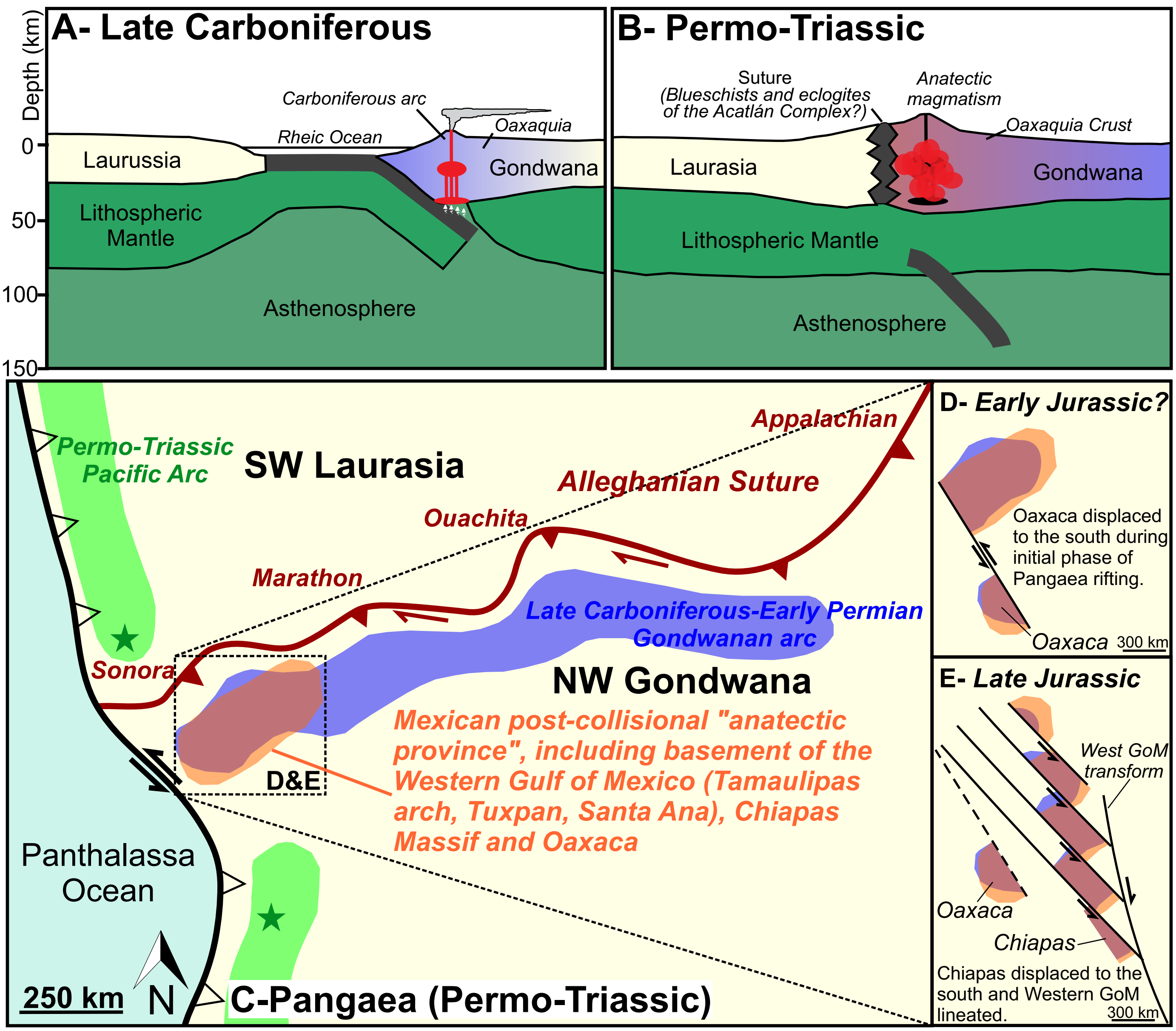

Henry Coombs; Figure 11; Manuscript 1

Click here to access/download
Supplemental File
Geochronology Appendix.xlsx